

ALMA Observations of Multiple-CO and C Lines Toward the Active Galactic Nucleus of NGC 7469: X-Ray-dominated Region Caught in the Act

TAKUMA IZUMI,^{1,2,*} DIEU D. NGUYEN,¹ MASATOSHI IMANISHI,^{1,2} TAIKI KAWAMURO,^{1,†} SHUNSUKE BABA,^{1,†}
SUZUKA NAKANO,² KOTARO KOHNO,^{3,4} SATOKI MATSUSHITA,⁵ DAVID S. MEIER,⁶ JEAN L. TURNER,⁷
TOMONARI MICHİYAMA,⁸ NANASE HARADA,⁵ SERGIO MARTÍN,^{9,10} KOUICHIRO NAKANISHI,^{1,2} SHURO TAKANO,¹¹
TOMMY WIKLIND,¹² NAOMASA NAKAI,^{13,14} AND PEI-YING HSIEH¹⁵

¹*National Astronomical Observatory of Japan, 2-21-1 Osawa, Mitaka, Tokyo 181-8588, Japan*

²*Department of Astronomical Science, The Graduate University for Advanced Studies, SOKENDAI, 2-21-1 Osawa, Mitaka, Tokyo 181-8588, Japan*

³*Institute of Astronomy, Graduate School of Science, The University of Tokyo, 2-21-1 Osawa, Mitaka, Tokyo 181-0015, Japan*

⁴*Research Center for the Early Universe, Graduate School of Science, The University of Tokyo, 7-3-1 Hongo, Bunkyo, Tokyo 113-0033, Japan*

⁵*Institute of Astronomy and Astrophysics, Academia Sinica 11F of Astronomy-Mathematics Building, AS/NTU, No.1, Sec.4, Roosevelt Rd., Taipei 10617, Taiwan, R.O.C.*

⁶*Department of Physics, New Mexico Institute of Mining and Technology, Socorro, NM 87801, USA*

⁷*UCLA Department of Physics and Astronomy, Los Angeles, CA 90095-1547, USA*

⁸*Kavli Institute for Astronomy and Astrophysics, Peking University, 5 Yiheyuan Road, Haidian District, Beijing 100871, P.R.China*

⁹*European Southern Observatory, Alonso de Córdova 3107, Vitacura, Santiago, 763-0355 Chile*

¹⁰*Joint ALMA Observatory, Alonso de Córdova, 3107, Vitacura, Santiago 763-0355, Chile*

¹¹*Department of Physics, General Studies, College of Engineering, Nihon University, Tamuramachi, Koriyama, Fukushima 963-8642, Japan*

¹²*Catholic University of America, Department of Physics, Washington, DC 20064, USA*

¹³*School of Science and Technology, Kwansei Gakuin University, 2-1 Gakuen, Sanda, Hyogo 669-1337, Japan*

¹⁴*Tomonaga Center for the History of the Universe, University of Tsukuba, Tsukuba, Ibaraki 305-8571, Japan*

¹⁵*Institute of Astronomy and Astrophysics, Academia Sinica 11F of Astronomy-Mathematics Building, AS/NTU, No.1, Sec.4, Roosevelt Rd., Taipei 10617, Taiwan, R.O.C.*

(Received May 18, 2020; Revised June 10, 2020; Accepted June 11, 2020)

Submitted to ApJ

ABSTRACT

We used the Atacama Large Millimeter/submillimeter Array (ALMA) to map $^{12}\text{CO}(J = 1-0)$, $^{12}\text{CO}(J = 2-1)$, $^{12}\text{CO}(J = 3-2)$, $^{13}\text{CO}(J = 2-1)$, and $[\text{C I}](^3P_1-^3P_0)$ emission lines around the type 1 active galactic nucleus (AGN) of NGC 7469 ($z = 0.0164$) at ~ 100 pc resolutions. The CO lines are bright in both the circumnuclear disk (central ~ 300 pc) and the surrounding starburst (SB) ring (~ 1 kpc diameter), with two bright peaks on either side of the AGN. By contrast, the $[\text{C I}](^3P_1-^3P_0)$ line is strongly peaked on the AGN. Consequently, the brightness temperature ratio of $[\text{C I}](^3P_1-^3P_0)$ to $^{13}\text{CO}(2-1)$ is ~ 20 at the AGN, as compared to ~ 2 in the SB ring. Our local thermodynamic equilibrium (LTE) and non-LTE models indicate that the enhanced line ratios (or C I enhancement) are due to an elevated C^0/CO abundance ratio ($\sim 3-10$) and temperature ($\sim 100-500$ K) around the AGN as compared to the SB ring (abundance ratio ~ 1 , temperature $\lesssim 100$ K), which accords with the picture of the X-ray-dominated Region (XDR). Based on dynamical modelings, we also provide CO(1-0)-to- and $[\text{C I}](^3P_1-^3P_0)$ -to-molecular mass conversion factors at the central ~ 100 pc of this AGN as $\alpha_{\text{CO}} = 4.1$ and $\alpha_{\text{CI}} = 4.4 M_{\odot} (\text{K km s}^{-1} \text{pc}^2)^{-1}$, respectively. Our results suggest that the C I enhancement is potentially a good marker of AGNs that could be used in a new submillimeter diagnostic method toward dusty environments.

Keywords: galaxies: active — galaxies: ISM — galaxies: evolution — ISM: molecules

1. INTRODUCTION

The cold gas, particularly in the molecular phase in the centers of galaxies, plays a key role in the evolution of galaxies because it is the site of massive star formation as well as the reservoir of fuel for central supermassive black holes (SMBHs). The mass accretion onto a SMBH produces enormous amounts of energy observable as an active galactic nucleus (AGN), which is much more efficient in producing X-ray radiation than massive stars (Hickox & Alexander 2018). Consequently, we would expect that such a different heating mechanism will produce different signatures on the circumnuclear gas properties (Meijerink & Spaans 2005; Meijerink et al. 2007). For example, photodissociation regions (PDRs) caused by intense ultra-violet (UV) radiation from massive stars (e.g., Hollenbach & Tielens 1997, 1999) likely give way to X-ray dominated regions (XDRs), where gas physical and chemical properties are governed by the harsh X-ray irradiation from the central AGN (e.g., Lepp & Dalgarno 1996; Maloney et al. 1996). Cosmic rays from supernovae and the injection of mechanical energy induced by AGN jet/outflow also make unique chemical compositions (e.g., Meijerink et al. 2011; Kazandjian et al. 2012, 2015).

Diagnosing these energy sources by sub/millimeter spectroscopic observations can be useful to uncover dust-obscured activity because these wavelengths do not suffer from severe dust extinction. For example, so-called obscured (total obscuring column $N_{\text{H}} \gtrsim 10^{23} \text{ cm}^{-2}$) AGNs account for $\gtrsim 50\%$ of the total AGN population at least at $z \sim 0-2$ (Buchner et al. 2015). Hence, a robust mm/submm energy diagnostics is quite beneficial to obtain a comprehensive picture on, e.g., the cosmic evolution of SMBHs.

Based on these interests, many key molecules have been suggested as useful observational diagnostic tools. Among them, an enhanced HCN intensity relative to those of CO, HCO^+ , or CS (e.g., Tacconi et al. 1994; Kohno et al. 2001; Kohno 2005; Krips et al. 2008; Izumi et al. 2013; Imanishi et al. 2007, 2016) may be a unique feature to AGNs. Extensive modelings of the observed line ratios suggest that an enhancement of HCN abundance would be a key to explain the intensity enhancement (Izumi et al. 2016b), which accords with the X-ray-induced chemistry (Lepp & Dalgarno 1996; Maloney et al. 1996) or with the chemistry rather generally expected in high temperature regions (Harada et al. 2010, 2013), although there are counter-arguments for

the reliability of this HCN-enhancement in AGNs (e.g., Costagliola et al. 2011; Privon et al. 2020). One difficulty of studying this HCN-enhancement is the interpretation of the ratio from the perspectives of line excitation, opacity, and particularly the complex (time-dependent) chemistry as discussed in Izumi et al. (2016b). Maser amplification of HCN intensity due to infrared-pumping may also matter (Matsushita et al. 2015). Hence, while keeping further investigation on the robust origin of the HCN-enhancement, another effort to explore alternative, and simpler to interpret if possible, sub/mm diagnostic methods is valuable.

Given this situation, here we focus on the submm atomic carbon emission line $[\text{C I}](^3P_1-^3P_0)$ (denoted as $[\text{C I}](1-0)$ hereafter) at the rest frequency of $\nu_{\text{rest}} = 492.1607 \text{ GHz}$. Because of the high abundance of C^0 atom and low energies of its fine structure levels from the ground state, the two lines of the $[\text{C I}]$ triplet are important coolant of the neutral interstellar medium (ISM). As C^0 is a very fundamental form of the carbon-bearing species, related formation and destruction processes are relatively simple to understand. In a classical PDR scheme, C^0 atoms distribute in a thin layer between a fully ionized H II region and a molecular core (Hollenbach & Tielens 1997, 1999). More recent refinements reached a general conclusion that C^0 rather co-exists with molecular CO due to, e.g., turbulent mixing (Glover et al. 2015), non-equilibrium chemistry (Stoerzer et al. 1997), influence of cosmic rays (Papadopoulos et al. 2004, 2018), or clumpiness (Meixner & Tielens 1993).

This global spatial concomitance has been confirmed in Galactic star-forming regions (e.g., Keene et al. 1997; Plume et al. 2000; Ikeda et al. 1999, 2002; Shimajiri et al. 2013). Although PDR surfaces cannot be resolved, such similar spatial distributions are also found in nearby starburst galaxies (Krips et al. 2016; Salak et al. 2019). These consequently constitute the basis for the use of $[\text{C I}](1-0)$ as a potential tracer of H_2 mass, and the line is now enthusiastically observed both in nearby (e.g., Papadopoulos & Greve 2004; Kamenetzky et al. 2012; Israel et al. 2015; Jiao et al. 2017; Crocker et al. 2019; Jiao et al. 2019) and high-redshift galaxies (e.g., Papadopoulos et al. 2004; Walter et al. 2011; Alaghband-Zadeh et al. 2013; Bothwell et al. 2017; Popping et al. 2017; Valentino et al. 2018, 2020; Nesvadba et al. 2019; Heintz & Watson 2020). Note that however, there is a distinct difference in, for example $[\text{C I}](1-0)/^{12}\text{CO}(1-0)$ line ratio between Galactic star-forming clouds and starburst galaxies. Central region of nearby starburst galaxies show $[\text{C I}](1-0)/^{12}\text{CO}(1-0) \sim 0.1 - 0.3$ (brightness temperature T_{B} unit; Gerin & Phillips 2000; Krips et al. 2016),

* NAOJ Fellow

† JSPS Fellow

whereas it is usually $\lesssim 0.1$ in Milky Way objects (e.g., Wright et al. 1991; Ojha et al. 2001; Oka et al. 2005) except for the harsh central molecular zone (CMZ) with $\sim 0.1 - 0.3$ (Ojha et al. 2001). Hence pertaining physical or chemical conditions would be different among these Galactic clouds and starburst galaxies.

As compared to PDRs, the higher column-penetrating power and higher dissociating/ionizing nature of X-rays will more efficiently enhance C^0 abundance in XDRs relative to CO over a larger volume of molecular cloud as the CO molecule is easily dissociated therein (Meijerink & Spaans 2005; Meijerink et al. 2007). Although most of the previous [C I](1–0) observations toward extragalactic objects were conducted with ground-based single-dish telescopes or *Herschel* Space Observatory that mixed up \gtrsim a few kpc scale emission (e.g., Gerin & Phillips 2000; Israel et al. 2015; Valentino et al. 2018), Israel & Baas (2002) showed that the ratio of [C I](1–0) to $^{13}\text{CO}(2-1)$, both of which would be optically thin, depends on a type of a galaxy: it is lowest for quiescent galaxies ($\lesssim 0.5 - 1$), moderate in starburst galaxies ($\sim 1 - 3$), and highest for AGN-host galaxies ($\sim 4 - 5$). The high [C I](1–0)/ $^{13}\text{CO}(2-1)$ ratio of $\sim 1 - 5$ (T_B unit), which is usually not seen in PDRs of our Galaxy (Keene et al. 1997), is at least partly attributed to elevated C^0 abundances in extragalactic nuclei via radiative transfer calculations. More recently, Izumi et al. (2018) found in the Circinus galaxy that [C I](1–0)/CO(3–2) flux ratio increases significantly when it is measured closer to the AGN position based on ALMA observations, indicating an influence of the AGN on the nature of the surrounding cold gas.

It is remarkable in this context that one-zone PDR and XDR models of Meijerink & Spaans (2005) show that the [C I](1–0)/ $^{13}\text{CO}(2-1)$ ratio can be $> 10\times$ higher in XDRs than in PDRs (Meijerink et al. 2007), due to the more efficient CO dissociation and more harsh excitation conditions in the former. However, such a distinct difference between AGNs and starburst galaxies was not observed in the single dish observations of Israel & Baas (2002). This could be due to their insufficient resolution to isolate XDRs, which have a characteristic size (diameter) of $\lesssim 100$ pc or $\lesssim 1''$ in the nearby universe (Schleicher et al. 2010). We thus need high resolution comprehensive observations of C^0 and CO lines to faithfully measure line flux (or abundance) ratios in XDRs, which then give a robust basis for the [C I](1–0)-based diagnostics. Now this can be accomplished by the Atacama Large Millimeter/submillimeter Array (ALMA), which provides unprecedented high angular resolutions and sensitivities.

1.1. The Target Galaxy NGC 7469

In this work we present high resolution ALMA observations of multiple CO and [C I](1–0) lines toward NGC 7469 (Figure 1) to study detailed line emission distributions and flux ratios, with our particular atten-

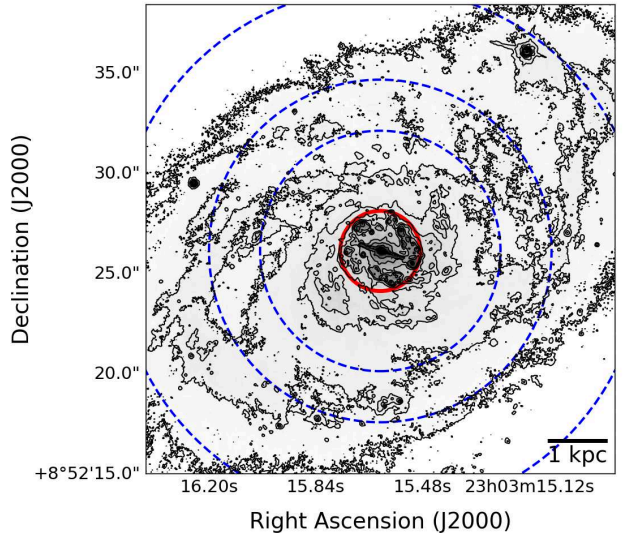


Figure 1. A *B*-band image of NGC 7469 acquired by the *Hubble Space Telescope* (*HST*) Advanced Camera for Surveys (ACS)/F435W. The gray scale and the contours only indicate counts. We extracted this data from the *HST* Legacy Archive. The regions of our interest, starburst ring and the circumnuclear disk, are encompassed by the red circle ($r = 2''$). The field of views (FoVs) of our ALMA observations are indicated by the blue dashed circles (smallest one = Band 8 FoV, then becomes larger for Band 7, 6...). Note that the central pixel (AGN) is saturated, hence the bar-like structure inside the red circle is an artifact.

tion on the [C I](1–0)/ $^{13}\text{CO}(2-1)$ ratio. NGC 7469 is an active barred spiral galaxy located at $D = 71.2$ Mpc ($z = 0.01641$ and $1'' = 334$ pc)¹. It hosts a luminous type-1 Seyfert nucleus with an absorption-corrected 2–10 keV luminosity of $L_{2-10\text{keV}} = 1.5 \times 10^{43}$ erg s^{−1} (Liu et al. 2014), as evidenced by broad Balmer emission lines (Peterson et al. 2014). The time-variability in UV to X-ray bands (Nandra et al. 2000; Kriss et al. 2000), as well as fast ionized outflows emanating from the nucleus (Blustin et al. 2007; Cazzoli et al. 2020) confirm the genuine existence of AGN in this galaxy. NGC 7469 is also categorized as luminous infrared galaxy (LIRG) owing to its high IR luminosity ($L_{8-1000\mu\text{m}} = 10^{11.6} L_{\odot}$, Sanders et al. 2003). There is a ~ 300 pc diameter circumnuclear disk (CND) at the center (e.g., Davies et al. 2004; Izumi et al. 2015), which is surrounded by a luminous starburst ring with a radius of ~ 500 pc (e.g., Soifer et al. 2003; Diaz-Santos et al. 2007). Relevant properties of NGC 7469 are summarized in Table 1.

¹ Based on the NASA/IPAC Extragalactic Database (NED). A standard cosmology of $H_0 = 70$ km s^{−1} Mpc^{−1}, $\Omega_M = 0.3$, and $\Omega_{\Lambda} = 0.7$ is assumed throughout this paper.

In the CND, multi-wavelength observations at centimeter (Lonsdale et al. 2003), *K*-band (Genzel et al. 1995), and $3.3 \mu\text{m}$ polycyclic aromatic hydrocarbon feature (Imanishi & Wada 2004; Esquej et al. 2014), all indicate that the AGN is energetically dominant. Reverberation mapping observations revealed that the mass of the central SMBH is $M_{\text{BH}} \sim 1 \times 10^7 M_{\odot}$ (Peterson et al. 2014), with an Eddington ratio of ~ 0.3 (Petrucci et al. 2004). The starburst ring is incredibly bright at various wavelengths including centimeter (Wilson et al. 1991; Orienti & Prieto 2010), submm (Izumi et al. 2015; Imanishi et al. 2016), far-infrared (FIR, Papadopoulos & Allen 2000), mid-infrared (MIR, Soifer et al. 2003; Díaz-Santos et al. 2007), near-infrared (NIR, Genzel et al. 1995; Scoville et al. 2000), and optical to UV (Malkan et al. 1998; Díaz et al. 2000; Colina et al. 2007), with an area-integrated star-formation rate (SFR) of as high as $\sim 30 - 50 M_{\odot} \text{ yr}^{-1}$ (Genzel et al. 1995; Pereira-Santaella et al. 2011). By jointly analyzing the multi-wavelength data, Díaz-Santos et al. (2007) revealed that many dusty, young ($< 100 \text{ Myr}$), and massive star clusters (individual mass $\sim 10^{6-7} M_{\odot}$) are embedded in the ring. Furthermore, low- J CO observations revealed the existence of a large amount of cold molecular gas ($> 10^9 M_{\odot}$) in the central $\lesssim 2 \text{ kpc}$ region (Meixner et al. 1990; Davies et al. 2004). We have secured efficient sub/mm observations toward this object thus far, indicating abundant molecular gas (Izumi et al. 2015, 2016a; Fathi et al. 2015). Therefore, NGC 7469 provides an optimal site to simultaneously investigate how AGN and starburst influence their surrounding gas when observed at high resolutions, and may also serve as a local template to better understand the ISM properties of high redshift quasars.

The structure of this paper is as follows. In § 2, we describe our ALMA observations. § 3 show the results of our observations including spatial distributions of the line emission, line profiles, and line ratios. We will discuss possible origins of enhanced ratios of [C I](1–0) to CO lines in § 4. A conversion factor from [C I](1–0)-to- and CO(1–0)-to- H_2 mass in the CND is also presented there. Our conclusions of this paper are summarized in § 5.

2. OBSERVATIONS AND DATA REDUCTION

Our aim of this program is to investigate detailed feedback of AGN and starburst activity on their surrounding medium. We observed multi-phase gas lines including the molecular lines $^{12}\text{CO}(1-0)$, $(2-1)$, $(3-2)$, an optically thin isotopologue $^{13}\text{CO}(2-1)$, and the atomic carbon [C I](1–0) line, as well as their underlying continuum emission by using ALMA. The relevant excitation parameters of these lines can be found in Table 2. Our observations were conducted during Cycle 5 (project ID: #2017.1.00078.S, PI = T. Izumi) using the Band 3, 6, 7, and 8 receivers, from 2017 December to 2018 September.

Table 1. Properties of NGC 7469

Parameter	Value	Ref.
(1)	(2)	(3)
RC3 morphology	(R')SAB(rs)a	(1)
Position of the nucleus		(2)
α_{ICRS}	$23^{\text{h}}03^{\text{m}}15^{\text{s}}.617$	
δ_{ICRS}	$+08^{\circ}52'26''.00$	
Position angle [$^{\circ}$]	128	(3)
Inclination angle [$^{\circ}$]	45	(3)
Systemic Velocity [km s^{-1}]	4920 ($z=0.01641$)	(2)
Distance [Mpc]	71.2	
Linear scale [pc arcsec^{-1}]	334	
Nuclear activity	Seyfert 1	(4)
$L_{2-10\text{keV}}$ [erg s^{-1}]	1.5×10^{43}	(5)
L_{IR} [L_{\odot}]	4×10^{11}	(6)
$\langle \text{SFR} \rangle$ (CND) [$M_{\odot} \text{ yr}^{-1} \text{ kpc}^{-2}$]	50–100	(7)
Stellar age (CND) [Myr]	110–190	(7)

NOTE—The $\langle \text{SFR} \rangle$ (CND) indicates the averaged star formation rate over the central $\sim 1''$ region (i.e., circumnuclear disk = CND). The stellar age is also measured for the CND. Kinematic parameters are derived based on CO observations. (1) de Vaucouleurs et al. (1991); (2) This work; (3) Davies et al. (2004); (4) Osterbrock & Martel (1993); (5) Liu et al. (2014); (6) Sanders et al. (2003); (7) Davies et al. (2007).

The phase-tracking center of single pointing was set to $(\alpha_{\text{J2000.0}}, \delta_{\text{J2000.0}}) = (23^{\text{h}}03^{\text{m}}15^{\text{s}}.617, +08^{\circ}52'26''.06\text{s})$, which was based on our previous ALMA observations at Band 7 (Izumi et al. 2015). Each receiver was tuned to cover one of the above-mentioned lines in the 2 sideband dual-polarization mode. Each spectral window has a bandwidth of 1.875 GHz, and two windows were placed to each sideband (upper and lower) to achieve a total frequency coverage of $\sim 7.5 \text{ GHz}$. We used two configurations of 12m arrays in Band 3 to 7 observations so that we can acquire both high angular resolutions sufficient to separate the starburst ring (radius $\sim 1''.5$) from the CND (radius $\sim 0''.5$) and recover the bulk of the emission extending over the central \sim a few arcsec scale. Note that, however, we decided not to use the compact configuration data of Band 7 observations as it would have issues in the calibration process. The Atacama Compact Array (ACA) was employed in the Band 8 observations for the same purpose: we did not include the total power array observations in this program. These result in the nominal maximum recoverable scales of our observations larger than $10''$. Owing to this, as well as to the fact that we will focus on line ratios measured

Table 2. The Line Excitation Parameters

Line	ν_{rest} (GHz)	E_u/k_B (K)	A_{ul} (s^{-1})	n_{cr} (cm^{-3})
$^{12}\text{CO}(1-0)$	115.2712	5.5	7.20×10^{-8}	2.1×10^3
$^{13}\text{CO}(2-1)$	220.3987	15.9	6.04×10^{-7}	9.7×10^3
$^{12}\text{CO}(2-1)$	230.5380	16.6	6.91×10^{-7}	1.1×10^4
$^{12}\text{CO}(3-2)$	345.7960	33.2	2.50×10^{-6}	3.6×10^4
[C I](1–0)	492.1607	23.6	7.88×10^{-8}	1.2×10^3

NOTE—Values are adopted from the LAMDA database (Schöier et al. 2005). E_u and k_B are the upper energy level from the ground state and the Boltzmann constant. The critical densities are calculated for $T_{\text{kin}} = 100$ K in the optically thin limit, simply as $n_{\text{cr}} = A_{ul}/C_{ul}$, where A_{ul} and C_{ul} are the Einstein A- and C-coefficients of a $u \rightarrow l$ transition. We only considered H_2 as a collision partner.

in several CO- or continuum-bright knots (i.e., compact structures), we do not consider effect of missing flux in this work. Further details of our observations are summarized in Table 3.

The reduction and calibration were done with CASA version 5.4 (McMullin et al. 2007) in the standard manner by using the CASA pipeline. The continuum emission was identified and subtracted in the uv -plane for each visibility set of different array configuration, and the resultant visibilities were properly combined by the task `concat`. All of the images presented in this paper were reconstructed using the task `clean` with the Briggs weighting. We applied the `robust` parameter of 0.0 to the Band 6, 7, and 8 datasets, which resulted in angular resolutions of $\sim 0''.34 - 0''.37$. As the same `robust` parameter produced a much higher resolution for the Band 3 data, we instead adopted `robust` = +0.5 with further tapering (`outertaper` = $0''.2$) to match its native beam size to the others as much as possible. The final achieved angular resolutions and 1σ sensitivities are listed in Table 4. Here the rms values were measured in channels free of line emission. Note that the channel spacings were originally 1.953 MHz (^{12}CO and ^{13}CO lines) and 3.906 MHz ([C I](1–0)), but we created cubes of ^{12}CO and [C I](1–0) lines with a common velocity resolution of $dV = 10$ km s^{-1} to improve the signal-to-noise (S/N) ratios. For the case of the $^{13}\text{CO}(2-1)$ cube, we adopted $dV = 20$ km s^{-1} due to the faintness of the line. In the following, we express velocities in the optical convention with respect to the local standard of rest. These data products were further analyzed with the MIRIAD software (Sault et al. 1995).

We also reconstructed five continuum maps by using each of the five datasets of different frequencies listed in Table 3. The rms values of these maps were measured in

areas free of emission. By inspecting the maps, we noticed that the notable peak positions (both in the CND and the starburst ring) of the Band 8 continuum map, as well as [C I](1–0) map, are offset by $\sim 0''.08$ ($\sim 20\%$ of the synthesized beam) toward the north-east direction relative to the corresponding positions in the other maps. This is due to a phase error in the Band 8 dataset, as confirmed by inspecting the position of a dedicated calibration source (quasar). For the analysis in the following, we corrected this positional offset. Note that in this work, we will use only the Band 7 (860 μm) continuum map to define representative locations to measure line fluxes. Details of the full continuum properties will be discussed elsewhere.

Throughout the paper, we use line intensities corrected for the primary beam attenuation for quantitative discussion, but this correction is not critical as most of the emission is within $r \lesssim 2''$ from the center, which is well smaller than the primary beams (see also Figure 1). We simply refer to the ^{12}CO isotopologue as CO, whereas ^{13}CO is explicitly identified. The atomic carbon species is denoted as C^0 , with its fine structure transition as [C I]. The pixel scale of ALMA images is set to $0''.06$, and the displayed errors indicate only statistical ones unless mentioned otherwise. As for the systematic error, the absolute flux calibration uncertainty is $\sim 10\%$ according to the Cycle 5 ALMA Proposer’s Guide.

3. RESULTS

3.1. Spatial distributions

We first describe the distribution of cold ISM traced by CO, ^{13}CO , and [C I] lines. Figure 2 shows the velocity-integrated intensity maps toward a central $6''$ (~ 2 kpc) boxy region of NGC 7469. We integrated a common velocity range of 4650–5200 km s^{-1} , which surely covers the line spectra at the nucleus (§ 3.2), without any clipping to make unbiased images, by using the MIRIAD task `moment`. The zeroth moment is defined as $I = dV \sum_i S_i$, where S is the line intensity and the summation is taken over the i th velocity channel of width dV . Properties of these maps can be found in Table 5. Emission of these lines were significantly detected both from the starburst ring (hereafter denoted as SB ring) and the CND (central $\sim 1''$), as well as the regions between or outside of them. Note that the SB ring is actually composed of two major spiral arms.

Among the multiple transitions of CO, $J = 1-0$ and $2-1$ lines are frequently used as a tracer of bulk molecular gas due to their low n_{cr} (Leroy et al. 2008, 2013). These lines are brighter at the CND than at the SB ring, manifesting a large amount of cold molecular gas in the CND. Contrary to this base distribution, we notice that the $^{13}\text{CO}(2-1)$ emission is significantly fainter at the CND than at the SB ring. Similar low intensities of ^{13}CO relative to ^{12}CO have been observed in SB systems with high FIR luminosities (e.g., Aalto et al. 1991, 1995; Henkel et al. 1998). As dis-

Table 3. Journal of Our ALMA Observations

Line	Date	Antenna	Baseline	Integration	Calibrator		
	(UT)	Number	(m)	(min)	Bandpass	Flux	Phase
(1)	(2)	(3)	(4)	(5)	(6)	(7)	(8)
$^{12}\text{CO}(1-0)$ (Band 3)	2017 Dec 07	46	41–3600	38	J2253+1608	J2253+1608	J2257+0743
	2018 Apr 25	42	15–500	15	J0006–0623	J0006–0623	J2257+0743
$^{13}\text{CO}(2-1)$ (Band 6)	2018 Jun 03	47	15–361	38	J2148+0657	J2148+0657	J2257+0743
	2018 Jun 08	43	15–314	24	J2253+1608	J2253+1608	J2257+0743
	2018 Sep 15	44	15–1261	55	J2253+1608	J2253+1608	J2257+0743
	2018 Sep 15	44	15–1261	54	J2253+1608	J2253+1608	J2257+0743
	2018 May 22	46	15–314	45	J2253+1608	J2253+1608	J2257+0743
$^{12}\text{CO}(2-1)$ (Band 6)	2018 Sep 14	43	15–1230	63	J2253+1608	J2253+1608	J2257+0743
	2018 Sep 14	43	15–1230	77	J2253+1608	J2253+1608	J2257+0743
	2018 Jul 16 [†]	47	15–314	3.5	J2253+1608	J2253+1608	J2232+1143
$^{12}\text{CO}(3-2)$ (Band 7)	2018 Sep 05	46	15–784	28	J2253+1608	J2253+1608	J2320+0513
	2018 Aug 22	48	15–484	85	J2253+1608	J2253+1608	J2232+1143
[C I](1–0) (Band 8)	2018 Aug 22	48	15–484	85	J2253+1608	J2253+1608	J2320+0513
	2018 May 12	10	9–49	50	J2258–2758	J2258–2758	J2253+1608
	2018 May 13	11	9–49	50	J2258–2758	J2258–2758	J2253+1608
	2018 May 19	12	9–49	50	J2258–2758	J2258–2758	J2253+1608
	2018 May 22	12	9–49	50	J2258–2758	J2258–2758	J2253+1608
	2018 May 23	12	9–49	50	J2258–2758	J2258–2758	J2253+1608
	2018 May 23	11	9–49	50	J2258–2758	J2258–2758	J2253+1608
	2018 May 25	11	9–49	50	J2258–2758	J2258–2758	J2253+1608
	2018 May 27	12	9–49	50	J2258–2758	J2258–2758	J2253+1608

NOTE—(1) observed line and the corresponding ALMA Band. (2) observing date in UT. (3) number of antennas used in the observation. (4) baseline length in meter. The minimum and maximum lengths are shown. (5) net on-source integration time in minute. (6)-(8) calibrators used in the observation. [†]This dataset was found to have serious issues in the calibration process. Given the short integration time that would not influence the overall properties of the $^{12}\text{CO}(3-2)$, we excluded this from our subsequent analysis.

Table 4. Achieved Cube Parameters

Emission	Beam ($'' \times ''$) ($^\circ$)	Beam (pc \times pc)	rms (mJy beam $^{-1}$)	dV (km s $^{-1}$)	Peak value (mJy beam $^{-1}$)
$^{12}\text{CO}(1-0)$	0.36×0.29 (-72.5°)	120×96	0.46	10	23.8
$^{13}\text{CO}(2-1)$	0.35×0.28 (41.2°)	117×92	0.13	20	10.0
$^{12}\text{CO}(2-1)$	0.37×0.30 (51.2°)	123×101	0.28	10	96.0
$^{12}\text{CO}(3-2)$	0.37×0.31 (-87.9°)	122×102	1.31	10	201
[C I](1–0)	0.34×0.31 (75.7°)	113×101	3.04	10	146
860 μm continuum	0.34×0.28 (-87.3°)	113×93	0.07	-	5.16

Table 5. Integrated Intensity Maps

Emission	Beam	rms
	(" × ")	(Jy beam ⁻¹ km s ⁻¹)
¹² CO(1–0)	0.36 × 0.29	0.034
	0.38	0.036
¹³ CO(2–1)	0.35 × 0.28	0.014
	0.38	0.015
¹² CO(2–1)	0.37 × 0.30	0.021
	0.38	0.025
¹² CO(3–2)	0.37 × 0.31	0.098
	0.38	0.118
[C I](1–0)	0.34 × 0.31	0.227
	0.38	0.245

NOTE—The velocity range of 4650–5200 km s⁻¹ was integrated to make these maps. Both the native resolution data and the common 0".38 resolution data are presented.

cussed in Miyamoto et al. (2018) for the case of the low-luminosity AGN NGC 613, we consider this faintness of ¹³CO(2–1) in NGC 7469 is due to a low optical depth of the emission (see § 4.1.2), and not due either to SB-induced selective photodissociation or nucleosynthesis (e.g., Langer et al. 1984; van Dishoeck & Black 1988; Matsushita et al. 1998): the latter two processes are inconsistent with the significantly lower star-formation activity in the CNB than in the SB ring (Esquej et al. 2014).

In Figure 2f we also show the distribution of the 860 μm (Band 7) continuum emission, which defines four representative positions (A–D) to measure line fluxes and extract spectra. The coordinates of these positions are listed in Table 6. The position-A coincides with the peak position of the Very Large Array 8.4 GHz (3.5 cm) continuum emission (Condon et al. 1991; Orienti & Prieto 2010) within ~ 0".1. We then regard this 860 μm peak position as the AGN position of NGC 7469. The 860 μm continuum distribution in the SB ring appears well consistent with those of MIR (Soifer et al. 2003), indicating that it traces thermal dust emission heated by young stars. Note however, we would need careful modelings of the continuum spectral energy distribution (SED) at the position-A to reveal its exact origin, as non-thermal synchrotron emission can be a severe contaminant even at Band 7, as observed in other galaxies (e.g., García-Burillo et al. 2014). Such modeling will be presented elsewhere.

In the SB ring all the line emission distributions peak at roughly the same positions as the 860 μm continuum

Table 6. Coordinates of the Peak Positions

Position	R.A.	Dec.
	(ICRS)	(ICRS)
A	23 ^h 03 ^m 15 ^s .617	+08°52'26".00
B	23 ^h 03 ^m 15 ^s .686	+08°52'27".02
C	23 ^h 03 ^m 15 ^s .581	+08°52'27".45
D	23 ^h 03 ^m 15 ^s .518	+08°52'25".02

emission, suggesting that these are star-forming giant molecular clouds (GMCs). On the other hand, there is a clear difference inside the CNB between the CO lines (both ¹²CO and optically thinner ¹³CO) and the [C I](1–0). The [C I](1–0) distribution clearly peaks at the exact AGN position, whereas CO lines have two bright knots at ~ 0".2 north and south to the AGN. This is not due to a slightly mismatched resolutions between the CO cubes and the [C I](1–0) cube. Indeed, we still see the same spatial difference after convolving the resolutions to a common 0".38 (Figure 3). Such a difference has not been the case in Galactic molecular clouds (e.g., Keene et al. 1997; Plume et al. 2000; Ikeda et al. 2002), nor in nearby SB galaxies (Krips et al. 2016; Salak et al. 2019), where global [C I](1–0) distribution resembles to those of low-*J* CO lines. As this resemblance provides the backbone for [C I](1–0) as a molecular mass tracer, our result may call into question its reliability near AGNs. Note that this relative faintness of the CO lines at the AGN positions is unlikely due to absorption effect, considering the type-1 Seyfert geometry where the AGN is directly visible.

Moreover, as compared to the CO and ¹³CO lines, this [C I](1–0) emission is more centrally-concentrated. For example, the relative fractions of the line fluxes measured at the central $r = 0".5$ circular region to those measured at the central $r = 3".0$ region are, $7.2 \pm 0.4\%$ for CO(1–0), $6.0 \pm 0.2\%$ for ¹³CO(2–1), $11.4 \pm 0.1\%$ for CO(2–1), $14.6 \pm 0.3\%$ for CO(3–2), but $20.0 \pm 0.7\%$ for [C I](1–0), respectively. The higher central concentration in CO(3–2) than CO(1–0) is a consequence of a higher gas excitation at the inner regions of galaxies. On the other hand, given the comparable n_{cr} (Table 2) of CO(1–0) and [C I](1–0), the significantly higher central concentration of the latter line stands out. We would need higher gas temperature (as the upper level energy is much higher for [C I](1–0) than for CO(1–0); Table 2) but also elevated C⁰ abundance around the AGN to explain this peculiar behavior. Given these different spatial distributions and central concentrations, we argue that the AGN influences the [C I](1–0) brightness likely in a form of XDR as discussed in § 4 (Maloney et al. 1996; Meijerink & Spaans 2005).

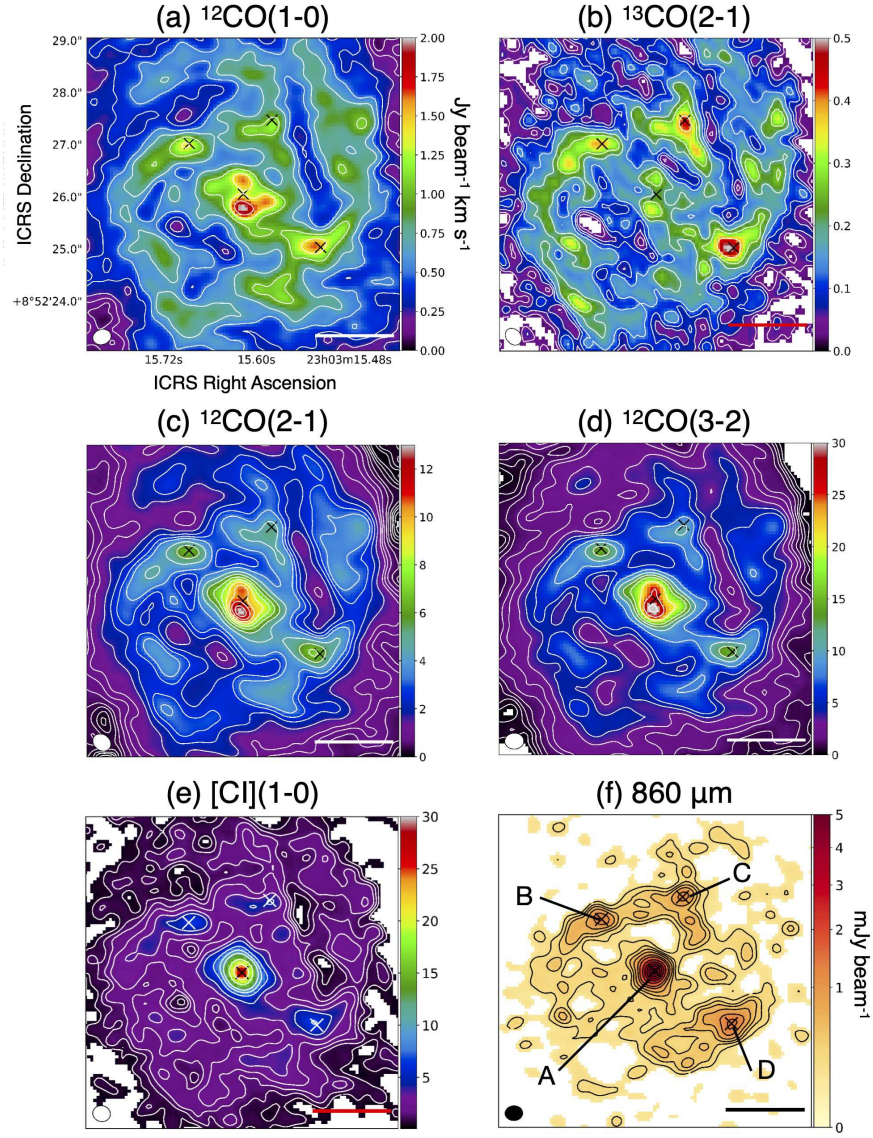


Figure 2. Integrated intensity maps of (a) $^{12}\text{CO}(1-0)$, (b) $^{13}\text{CO}(2-1)$, (c) $^{12}\text{CO}(2-1)$, (d) $^{12}\text{CO}(3-2)$, and (e) $[\text{C I}](1-0)$, in the central ~ 2 kpc region of NGC 7469, shown in the $\text{Jy beam}^{-1} \text{ km s}^{-1}$ unit. The common velocity range integrated over is $4650\text{--}5200 \text{ km s}^{-1}$ for all line emission maps. The $860 \mu\text{m}$ continuum emission map (mJy beam^{-1} unit) is also shown in the panel (f) to define the four representative positions (A–D; shown by the crosses in each panel), where we measure line fluxes and spectra. The position-A corresponds to the AGN position of this galaxy. In the emission line maps, contours are drawn at $3, 5, 7, 10, 15, 20, 30, 40, 50, 75, 100, 125, 150, 200, 250, 300, 350, \dots, 600,$ and $650 \times \sigma$ levels (1σ values are listed in Table 5). The bottom-left filled ellipses indicate the synthesized beams and the horizontal bar in each panel corresponds to 500 pc length. Note that the native resolution maps are shown here, whereas we convolve these maps to a common $0.38''$ resolution to take line ratios. The signals below 1.5σ are masked to enhance the clarity.

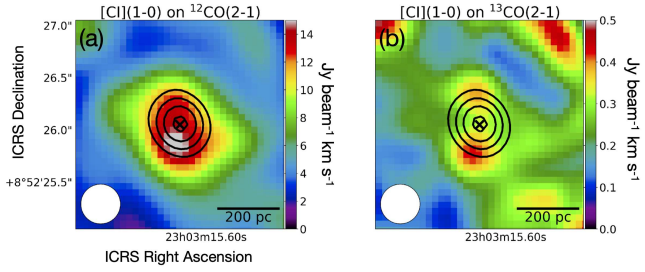


Figure 3. Closed-up view of the CND. The color scales indicate (a) CO(2–1) and (b) $^{13}\text{CO}(2-1)$ distributions, respectively. The 1σ rms values are 0.025 (a) and 0.015 (b) $\text{Jy beam}^{-1} \text{ km s}^{-1}$, respectively. Also plotted contours indicate [C I](1–0) distribution (70, 80, 90, ..., 130σ , where $1\sigma = 0.245 \text{ Jy beam}^{-1} \text{ km s}^{-1}$). These emissions are mapped at a common $0''.38$ resolution. The central cross in each panel defines the AGN location (position-A).

3.2. Spectra and Channel maps

Figure 4 compares the line spectra at the positions A–D measured with the common $0''.38$ ($\sim 130 \text{ pc}$) aperture. Note that the flux densities of CO(1–0) and $^{13}\text{CO}(2-1)$ are multiplied by certain factors to fit into the panels due to their faintness. The lines are much broader at the position-A (full-width at zero-intensity FWZI $\sim 450 \text{ km s}^{-1}$) than at the B–D (FWZI $\sim 150 - 200 \text{ km s}^{-1}$). The different line widths indicate a higher turbulence at the position-A where the AGN reside than the rest positions, as well as likely higher enclosed mass within the aperture therein.

The CO and ^{13}CO line profiles at the position-A clearly deviate from a single Gaussian, having two peaks at $V_{\text{LSR}} \sim 4850 \text{ km s}^{-1}$ and $V_{\text{LSR}} \sim 4980 \text{ km s}^{-1}$. The [C I](1–0) profile also shows a deviation from a single Gaussian but with a less-prominent higher-velocity peak than the CO lines. The lower-velocity peak of the [C I](1–0) line profile comes at around $V_{\text{LSR}} \sim 4900 \text{ km s}^{-1}$, which is offset to those of the CO lines. Such different line profiles between CO lines and [C I](1–0) have not been clearly observed in, e.g., a SB galaxy NGC 1808 (Salak et al. 2019) and the Large Magellanic Cloud (Okada et al. 2019). This difference is due to the different gas distributions in the velocity space as can be seen in the line channel maps (Figure 5; we present only the [C I](1–0) and the CO(2–1) maps for simplicity).

From the channel maps, it is evident that the [C I](1–0) shows a rotating structure around the AGN, and peaks exactly at the AGN position at $V_{\text{LSR}} \sim 4920 \text{ km s}^{-1}$, whereas CO(2–1) does not show such a clear peak at the AGN. This velocity (4920 km s^{-1}) is roughly the average of the two peak velocities of the CO line profiles fitted with a double-Gaussian function (see Table 7). It is also consistent with the previous estimate on the systemic velocity (V_{sys}) of NGC 7469 (Meixner et al.

1990), who defined V_{sys} as the line center of a CO(1–0) profile (4925 km s^{-1}). Given the higher resolution and the higher S/N ratio we obtained than previous sub/mm works, as well as our suggestion that the [C I](1–0) brightness would reflect the AGN influence (§ 4.1), we decide to adopt the above $V_{\text{LSR}} = 4920 \text{ km s}^{-1}$ ($z = 0.01641$) as an updated V_{sys} throughout this work. This number is exactly the same as the V_{sys} that we dynamically estimate (§ 4.2).

We determine the line peak flux density, centroid velocity, full-width at half-maximum (FWHM), line flux, and line luminosity, by fitting a Gaussian function to the observed spectra. The results are summarized in Table 7. Here we assumed a single Gaussian profile for the lines at the positions B–D, but we used a double Gaussian profile for those at the position-A, by taking the observed profiles into account. The line luminosity is calculated as

$$\left(\frac{L'_{\text{line}}}{\text{K km s}^{-1} \text{ pc}^2} \right) = 3.25 \times 10^7 \left(\frac{D_L}{\text{Mpc}} \right)^2 \left(\frac{\nu_{\text{rest}}}{\text{GHz}} \right)^{-2} \times (1+z)^{-1} \left(\frac{S\Delta V}{\text{Jy km s}^{-1}} \right), \quad (1)$$

where $S\Delta V$ is the line flux and D_L is the luminosity distance (Solomon & Vanden Bout 2005). The line luminosity is also computed in the unit of L_{\odot} as

$$\left(\frac{L_{\text{line}}}{L_{\odot}} \right) = 1.04 \times 10^{-3} \left(\frac{\nu_{\text{rest}}}{\text{GHz}} \right) (1+z)^{-1} \left(\frac{S\Delta V}{\text{Jy km s}^{-1}} \right) \left(\frac{D_L}{\text{Mpc}} \right)^2 \quad (2)$$

In the SB ring, each line shows comparable fluxes among the positions B–D, implying similar ISM conditions therein. In terms of the line luminosity (L_{\odot} unit), CO(3–2) clearly overwhelms the others, and [C I](1–0) follows. The FWHM of the [C I](1–0) is close to those of the CO(1–0) and $^{13}\text{CO}(2-1)$, i.e., low excitation line or optically thin line. These FWHMs are smaller than those of the CO(2–1) and (3–2) lines. As the gas density is usually high ($\gtrsim 10^4 \text{ cm}^{-3}$) in the central kpc regions of galaxies (e.g., Viti et al. 2014), one potential reason for these different line FWHMs is an opacity broadening (saturation effect) as bulk of the CO molecules can be excited to higher- J levels.

In the CND (position-A), there are clearly CO-weak and C⁰-prominent velocity channels at around $V_{\text{LSR}} \sim 4900 \text{ km s}^{-1}$. Hence a special care would be required when we take line ratios at this AGN position. We found that both the lower-velocity component and the higher-velocity one have comparable line fluxes and FWHMs for the cases of the CO and ^{13}CO lines. On the other hand, the lower-velocity component, which is closer to our V_{sys} , is much brighter and wider for the case of the [C I](1–0) line. It is also noteworthy that the [C I](1–0)

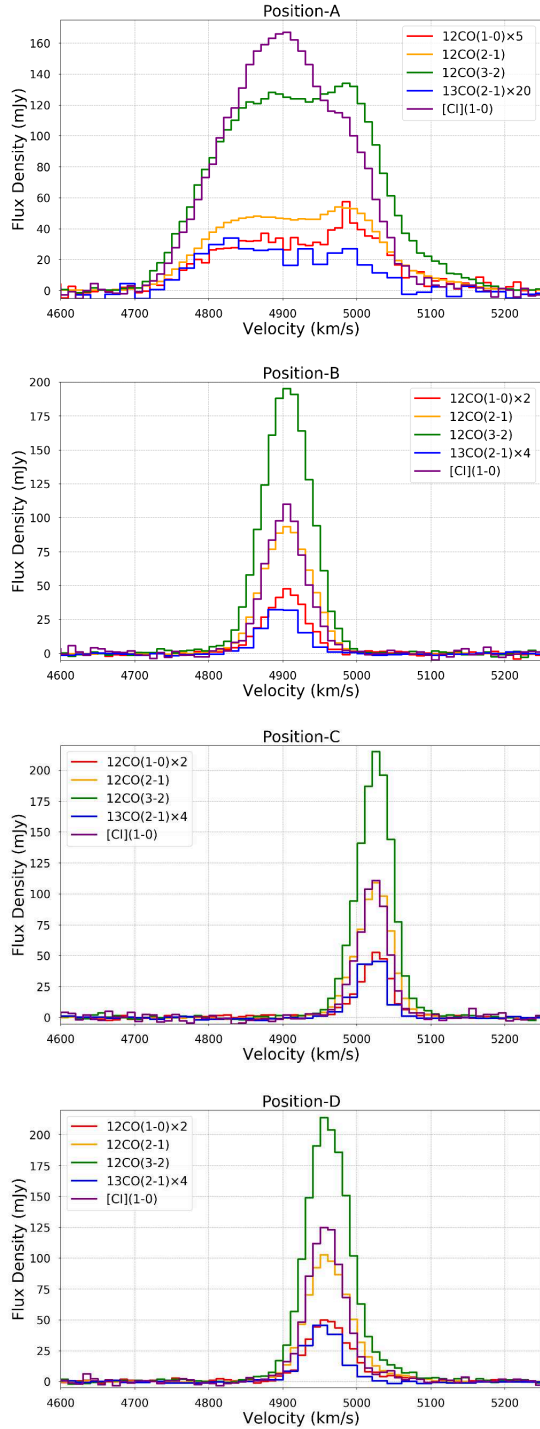


Figure 4. Continuum-subtracted spectra of $^{12}\text{CO}(1-0)$, $(2-1)$, $(3-2)$, $^{13}\text{CO}(2-1)$, and $[\text{C I}](1-0)$ extracted with the common $0''.38$ (~ 130 pc) aperture placed at the positions A–D (see Figure 2). Due to the faintness, $^{12}\text{CO}(1-0)$ and $^{13}\text{CO}(2-1)$ spectra are scaled by certain factors for a demonstrative purpose.

line luminosity (L_{\odot} unit) is outstandingly high at this position: L_{line} of $[\text{C I}](1-0)$ is $(8.2 \pm 0.2) \times 10^4 L_{\odot}$ after summing up both the low and high velocity components, while it is $(7.6 \pm 0.1) \times 10^4 L_{\odot}$ even after adding all the CO and ^{13}CO line luminosities observed here. Hence $[\text{C I}](1-0)$ contributes to the ISM cooling as significant as low- J CO lines, implying that the chemical composition is different at this position-A as compared to the other positions in the SB-ring.

3.3. The $[\text{C I}](1-0)$ diagnostics

By using the results of the Gaussian fitting (Table 7), we measure line flux ratios² at the positions A–D. At the position-A, we use the combined flux of the low and high velocity components for simplicity. Hence the ratios at that position reflect an averaged property over the $0''.38$ (~ 130 pc) area. Selected channel map-based values will also be shown in the following.

We here investigate $[\text{C I}](1-0)/\text{CO}(2-1)$ ($\equiv R_{\text{CI}/\text{CO}}$) and $[\text{C I}](1-0)/^{13}\text{CO}(2-1)$ ($\equiv R_{\text{CI}/^{13}\text{CO}}$) T_{B} ratios based on our motivation to study XDR effects on the surrounding gas, including the dissociation of CO molecules. A dependence of $R_{\text{CI}/^{13}\text{CO}}$ on the environments (PDR vs XDR) has been discussed both in observational works (Israel & Baas 2002; Israel et al. 2015) and in chemical models (Meijerink et al. 2007). Both $[\text{C I}](1-0)$ and $^{13}\text{CO}(2-1)$ lines are expected to be at least moderately optically thin under a wide range of physical conditions that would be valid for nearby galaxies. Hence their ratio is highly sensitive not only to excitation conditions but also to their abundances. CO(2-1) line has a $\sim 10\times$ higher n_{cr} than $[\text{C I}](1-0)$ in the optically thin limit, but its effective n_{cr} after accounting for photon trapping effects would be comparable to the n_{cr} of $[\text{C I}](1-0)$ (Salak et al. 2019). Hence $R_{\text{CI}/\text{CO}}$ may also be sensitive to an abundance ratio, although the excitation and opacity effects should be carefully considered.

These line ratios at the positions A–D are summarized in Table 8. The line ratios are comparable at the positions B–D: we also found that their $R_{\text{CI}/\text{CO}}$ are comparable to that found in the central region of the nearby SB galaxy NGC 253 (Krips et al. 2016) after assuming $T_{\text{CO}(1-0)} = T_{\text{CO}(2-1)}$. On the other hand, both ratios are significantly higher at the position-A. The $R_{\text{CI}/\text{CO}}$ and $R_{\text{CI}/^{13}\text{CO}}$ at the position-A are $\sim 2.5\times$ and $\sim 9\times$ higher than the values in the SB ring, respectively. In addition to these, we measured channel-based line ratios at the position-A, for example at the channel of 4900 km s^{-1} that shows the brightest $[\text{C I}](1-0)$ emission (Figure 4), to better reflect the different line profiles we observed. Now the ratios become even higher: the $R_{\text{CI}/\text{CO}}$ and $R_{\text{CI}/^{13}\text{CO}}$ at the position-A are $\sim 4\times$ and $\sim 11\times$ higher than the SB ring values, respectively. Therefore,

² We express line ratios in the brightness temperature (T_{B}) unit with the Rayleigh-Jeans approximation.

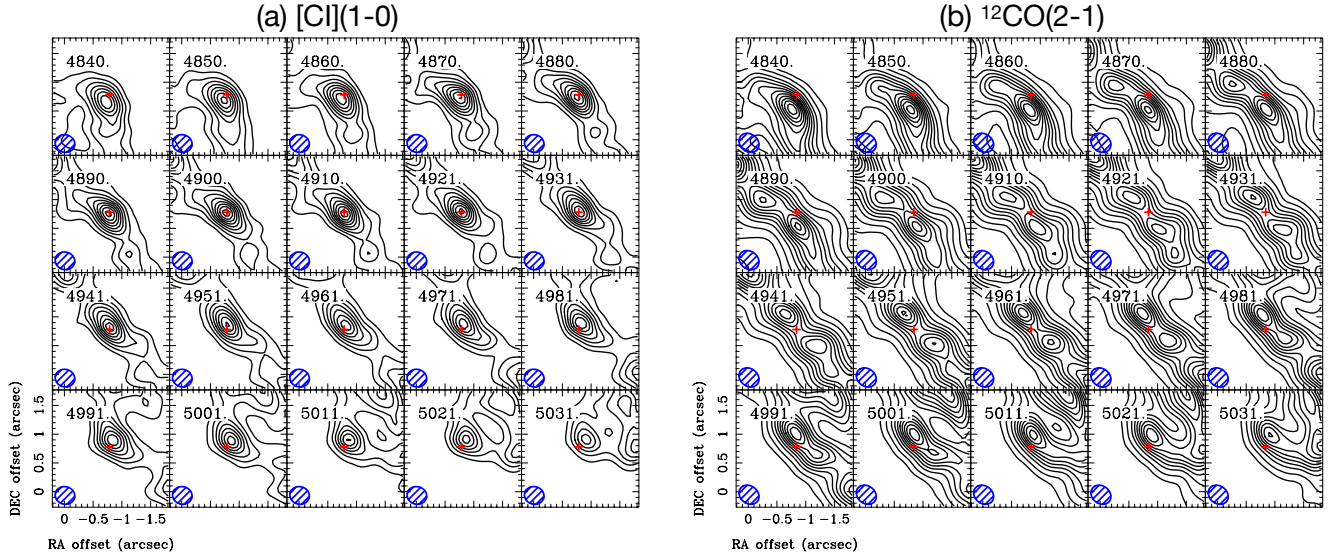


Figure 5. Velocity channel maps of (a) [C I](1–0) and (b) $^{12}\text{CO}(2-1)$ line emission in the central $2'' \times 2''$ ($1'' = 334$ pc) region of NGC 7469. The red plus indicates the AGN position. The synthesized beam is plotted in the bottom-left corner. Contours are drawn at 5, 10, 15, ..., 45 σ levels ($1\sigma = 3.04$ mJy beam $^{-1}$) for (a), and 10, 25, 50, 75, ..., 300 σ levels ($1\sigma = 0.28$ mJy beam $^{-1}$) for (b), respectively. Note that the positional offsets are relative to the phase reference center, which is not identical to the AGN position. At $V_{\text{LSR}} \sim 4920$ km s $^{-1}$ the peak position of the [C I](1–0) line distribution coincides with the exact AGN position.

it is evident that the [C I](1–0) flux is dramatically enhanced relative to the CO and ^{13}CO fluxes around the AGN as compared to the cases in the SB ring.

We have also listed single dish (SD)-based flux ratios of NGC 7469 in Table 8, which are taken from Israel et al. (2015). These values are obtained by the *Herschel* satellite and the ground-based James Clerk Maxwell Telescope after matching the resolutions to the *Herschel* data ($\sim 35''$). However, as the bright sources of the molecular line emission are the CND and the SB ring (Davies et al. 2004), the SD-based ratios basically reflect the averaged ISM properties of these structures. Indeed, the SD values are intermediate between the ALMA-based values at the position-A and B–D. It is therefore worth emphasizing that the $R_{\text{CI}/^{13}\text{CO}}$ of NGC 7469 (AGN) is $> 5\times$ higher than the SD-based ratio. This manifests the power and the necessity of the high angular resolutions provided by ALMA to spatially separate the regions with different heating sources, in particular a compact AGN-influenced region from extended SB regions, to measure line ratios that reflect the environment properly.

To compare the observed line ratios in NGC 7469 with those of other galaxies with various nuclear activities, we again compiled line flux data of [C I](1–0), CO(2–1), and $^{13}\text{CO}(2-1)$ from Israel et al. (2015). The literature data was taken with ground-based single dish telescopes with apertures of $> 22''$ (see their Table 5), hence basically probes spatial scales of $>$ several kpc. Their sample includes AGNs (NGC 1068, NGC

3079, NGC 4736, NGC 4945, M51, and the Circinus galaxy), SB galaxies (IC 10, NGC 253, NGC 660, IC 342, Henize 2–10, NGC 3628, NGC 4038, M83, and NGC 6946; these include low-ionization nuclear emission-line region (LINER) type galaxies as well), and quiescent galaxies (NGC 278, NGC 891, Maffei 2). Our classification of the nuclear type is based on the record in the NED database except for IC 10 and Maffei 2; we classified these as SB given their high nuclear star-formation rates (Mateo 1998; Meier et al. 2008).

The resultant plot of $R_{\text{CI}/\text{CO}}$ vs $R_{\text{CI}/^{13}\text{CO}}$ is displayed in Figure 6. At first inspection, although the physical scales probed are different, one may see that some galaxies with AGN contribution tend to have higher ratios in both axes. The SB galaxies, as well as the SB ring of NGC 7469, are all clustered around $R_{\text{CI}/\text{CO}} \sim 0.2 - 0.3$ and $R_{\text{CI}/^{13}\text{CO}} \sim 2 - 4$: physical and/or chemical conditions governing these regions/environments (e.g., PDR characteristics) are thus not likely different dramatically. While some SD-based AGN ratios are already significantly higher than those of the SB galaxies, our ALMA-based ratios of NGC 7469 AGN, particularly the channel map-based values, are outstandingly high in both $R_{\text{CI}/\text{CO}}$ and $R_{\text{CI}/^{13}\text{CO}}$.

In summary, to our best knowledge, these high ratios of NGC 7469 (AGN), or called as *C I-enhancement* hereafter, have never been observed in SB galaxies or quiescent galaxies at the spatial scales probed here. Thus, we now consider that this diagram has a potential to

Table 7. Results of the Gaussian fitting

		A	B	C	D
$^{12}\text{CO}(1-0)$	Peak (mJy)	$6.6 \pm 0.2, 8.1 \pm 0.3$	22.6 ± 0.3	25.4 ± 0.3	24.9 ± 0.3
	Line center (km s^{-1})	$4862.0 \pm 4.6, 5003.2 \pm 2.8$	4909.2 ± 0.4	5030.3 ± 0.3	4966.8 ± 0.3
	FWHM (km s^{-1})	$149.7 \pm 9.5, 107.1 \pm 5.3$	67.4 ± 0.9	48.3 ± 0.7	67.5 ± 0.8
	Flux (Jy km s^{-1})	$1.0 \pm 0.1, 0.9 \pm 0.1$	1.6 ± 0.1	1.3 ± 0.1	1.7 ± 0.1
	L'_{line} ($10^6 \text{ K km s}^{-1} \text{ pc}^2$)	$12.3 \pm 0.9, 10.9 \pm 0.7$	19.0 ± 0.3	15.3 ± 0.3	20.9 ± 0.3
	L_{line} ($10^2 L_{\odot}$)	$6.0 \pm 0.4, 5.3 \pm 0.4$	9.3 ± 0.2	7.5 ± 0.1	10.2 ± 0.2
$^{13}\text{CO}(2-1)$	Peak (mJy)	$1.6 \pm 0.1, 1.2 \pm 0.1$	8.7 ± 0.1	12.8 ± 0.1	11.8 ± 0.1
	Line center (km s^{-1})	$4842.8 \pm 5.1, 4981.9 \pm 6.8$	4909.2 ± 0.4	5030.0 ± 0.2	4964.2 ± 0.3
	FWHM (km s^{-1})	$113.5 \pm 11.2, 113.1 \pm 14.8$	58.8 ± 0.9	44.2 ± 0.5	56.3 ± 0.6
	Flux (Jy km s^{-1})	$0.19 \pm 0.02, 0.14 \pm 0.02$	0.52 ± 0.01	0.57 ± 0.01	0.67 ± 0.01
	L'_{line} ($10^6 \text{ K km s}^{-1} \text{ pc}^2$)	$0.63 \pm 0.07, 0.47 \pm 0.07$	1.7 ± 0.1	1.9 ± 0.1	2.2 ± 0.1
	L_{line} ($10^2 L_{\odot}$)	$2.2 \pm 0.2, 1.6 \pm 0.2$	6.0 ± 0.1	6.6 ± 0.1	7.7 ± 0.1
$^{12}\text{CO}(2-1)$	Peak (mJy)	$45.2 \pm 0.2, 50.3 \pm 0.2$	93.7 ± 0.2	106.1 ± 0.2	101.5 ± 0.2
	Line center (km s^{-1})	$4847.7 \pm 0.6, 4988.2 \pm 0.6$	4910.7 ± 0.1	5029.1 ± 0.1	4966.2 ± 0.1
	FWHM (km s^{-1})	$133.2 \pm 1.0, 137.0 \pm 0.9$	76.3 ± 0.2	54.4 ± 0.1	69.1 ± 0.1
	Flux (Jy km s^{-1})	$6.1 \pm 0.1, 7.0 \pm 0.1$	7.3 ± 0.1	5.9 ± 0.1	7.1 ± 0.1
	L'_{line} ($10^6 \text{ K km s}^{-1} \text{ pc}^2$)	$18.7 \pm 0.2, 21.4 \pm 0.2$	22.2 ± 0.1	17.9 ± 0.1	21.8 ± 0.1
	L_{line} ($10^2 L_{\odot}$)	$73.3 \pm 0.6, 83.9 \pm 0.7$	87.1 ± 0.2	70.3 ± 0.2	85.4 ± 0.2
$^{12}\text{CO}(3-2)$	Peak (mJy)	$114.0 \pm 1.4, 118.4 \pm 1.7$	197.3 ± 0.8	210.6 ± 1.0	213.7 ± 0.9
	Line center (km s^{-1})	$4856.7 \pm 1.7, 4990.3 \pm 1.5$	4910.9 ± 0.2	5029.9 ± 0.1	4966.0 ± 0.1
	FWHM (km s^{-1})	$145.3 \pm 2.5, 133.7 \pm 2.1$	75.8 ± 0.4	54.3 ± 0.3	68.3 ± 0.3
	Flux (Jy km s^{-1})	$16.8 \pm 0.4, 16.1 \pm 0.3$	15.2 ± 0.1	11.6 ± 0.1	14.8 ± 0.1
	L'_{line} ($10^6 \text{ K km s}^{-1} \text{ pc}^2$)	$22.9 \pm 0.5, 21.9 \pm 0.5$	20.7 ± 0.1	15.8 ± 0.1	20.2 ± 0.1
	L_{line} ($10^2 L_{\odot}$)	$302.9 \pm 6.3, 289.5 \pm 6.2$	273.5 ± 1.7	209.1 ± 1.5	270.0 ± 1.6
[C I](1-0)	Peak (mJy)	$167.0 \pm 1.2, 39.3 \pm 3.3$	105.3 ± 1.8	109.7 ± 2.1	126.6 ± 1.9
	Line center (km s^{-1})	$4898.8 \pm 1.3, 5008.2 \pm 1.7$	4908.4 ± 0.5	5027.2 ± 0.4	4963.3 ± 0.4
	FWHM (km s^{-1})	$173.0 \pm 2.7, 63.5 \pm 5.6$	65.1 ± 1.3	46.4 ± 1.0	57.8 ± 1.0
	Flux (Jy km s^{-1})	$29.4 \pm 0.5, 2.5 \pm 0.3$	7.0 ± 0.2	5.2 ± 0.2	7.4 ± 0.2
	L'_{line} ($10^6 \text{ K km s}^{-1} \text{ pc}^2$)	$19.7 \pm 0.3, 1.7 \pm 0.2$	4.7 ± 0.1	3.5 ± 0.1	5.0 ± 0.1
	L_{line} ($10^2 L_{\odot}$)	$751.7 \pm 12.9, 64.9 \pm 7.9$	178.3 ± 4.7	132.5 ± 4.0	190.5 ± 4.4

NOTE— These values are measured at the four 860 μm continuum peak positions (A–D; Figure 2) with the common $0''.38$ ($\sim 130 \text{ pc}$) aperture. The systematic uncertainties are not included in the flux values. At the position-A, we performed double Gaussian fittings considering the observed line profiles (Figure 4).

discriminate nuclear activities, as a submm energy diagnostic tool.

4. DISCUSSION

In this section we investigate a physical origin of the C I-enhancement revealed in § 3.3 by performing both local thermodynamic equilibrium (LTE) and non-LTE analyses of $R_{\text{C I}/\text{CO}}$ and $R_{\text{C I}/^{13}\text{CO}}$. The purpose of these analyses is to understand a trend of the underlying physical and/or chemical conditions to explain the C I-

enhancement. Further detailed non-LTE modeling with extensive comparison with chemical models will be presented in our forthcoming paper.

One will later see in this section that an elevated C^0 abundance is required to explain the C I-enhancement at the AGN position of NGC 7469. This calls a tension in molecular mass measurements using this line, particularly those at the CN scale of AGN-host galaxies. Therefore, we dedicate § 4.2 to derive a specific

Table 8. [C I](1–0)-related line ratios (T_B unit)

Position	[C I](1–0)/CO(2–1)	[C I](1–0)/ ¹³ CO(2–1)
A	0.53 ± 0.08	19.5 ± 3.3
B	0.21 ± 0.03	2.68 ± 0.39
C	0.19 ± 0.03	1.81 ± 0.26
D	0.23 ± 0.03	2.22 ± 0.32
A (ch) [†]	0.78 ± 0.11	25.1 ± 4.4
SD [‡]	0.30 ± 0.06	3.63 ± 0.77

NOTE—All ratios are taken with the common 0".38 aperture and include the systematic flux uncertainties. [†]Channel map-based line ratios at the position-A. We measured these ratios at $V_{LSR} = 4900 \text{ km s}^{-1}$, i.e., at the channel where the [C I](1–0) becomes brightest. [‡]Ratios measured with single dish (SD) observations (Israel et al. 2015).

[C I](1–0) to M_{H_2} (and CO(1–0) to M_{H_2}) conversion factor based on our dynamical modeling.

4.1. Physical origin of the CI-enhancement

4.1.1. LTE perspective

We begin by calculating $R_{CI/13CO}$ under optically thin LTE conditions to relate the flux ratio to C^0/CO column density ratios (N_{C^0}/N_{CO}). As these lines are likely optically thin or moderately opaque at the most physical conditions, as well as their n_{cr} are modest, we consider that both optically thin and LTE conditions are good approximations for a first-order estimation. From equations (1) and (2) of Tauber et al. (1995), we can describe the line flux ratio as

$$R_{CI/13CO} = 0.006 A_{13}^{12} f(T_{ex}) \times N_{C^0}/N_{CO}, \quad (3)$$

where

$$f(T_{ex}) = T_{ex}/(e^{7.0/T_{ex}} + 3e^{-16.6/T_{ex}} + 5e^{-55.5/T_{ex}}) \quad (4)$$

with T_{ex} and A_{13}^{12} denoting an excitation temperature (assumed to be common for all species) and an isotopic abundance ratio of [CO]/[¹³CO], respectively. Hereafter [X] means an abundance of the species X. The isotopic ratio varies significantly from galaxy to galaxy, and even inside a single galaxy (e.g., Milam et al. 2005). For example, A_{13}^{12} (we assume that this is identical to [¹²C]/[¹³C] here) is $\sim 50 - 60$ at inner Galactic sources (Lucas & Liszt 1998), ~ 25 in the Galactic central region (Gusten et al. 1985), and > 40 in nearby SB galaxies (Martín et al. 2010; Henkel et al. 2014; Tang et al. 2019)³. Recently, Tang et al. (2019) measured this ra-

³ But see also Martín et al. (2019) for a smaller value of $A_{13}^{12} \sim 21$ observed in the SB galaxy NGC 253.

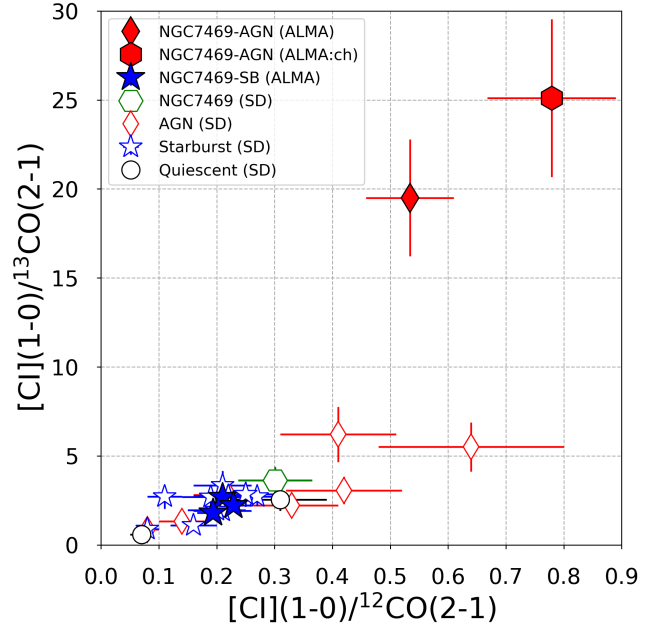


Figure 6. [C I](1–0)/¹²CO(2–1) = $R_{CI/CO}$ vs [C I](1–0)/¹³CO(2–1) = $R_{CI/13CO}$ line flux ratios (T_B scale). Our ALMA results of NGC 7469 are shown with the filled symbols, while single dish (SD) measurements are shown with the open symbols. The red diamonds, blue stars, black circles respectively indicate the data of AGN, SB galaxies, and quiescent galaxies. We also show the channel map-based ratios of the NGC 7469 AGN by the filled red hexagon. The SD measurements of NGC 7469 is also shown by the open green hexagon. Galaxies other than NGC 7469 (ALMA) are compiled from Israel et al. (2015), all of which are based on SD observations. AGNs tend to have higher values in both ratios, but even among them the extremely high values of NGC 7469 (AGN) and NGC 7469 (AGN: ch) stand out.

tio in the type-2 Seyfert galaxy NGC 1068, which has a similar AGN luminosity to NGC 7469. As it is impractical to determine the isotopic ratio in NGC 7469 with the current dataset, we assume $A_{13}^{12} = 40$ hereafter, which is roughly the same value found in NGC 1068 (~ 38). Note that, based on the equation (3), $R_{CI/13CO}$ linearly depends on the assumed A_{13}^{12} .

By using the equations (3) and (4), we calculate the $R_{CI/13CO}$ as a function of T_{ex} , for varying N_{C^0}/N_{CO} , in Figure 7. Under these conditions, it is evident that the $R_{CI/13CO}$ observed in the SB ring of NGC 7469 and other SB galaxies can be explained by $N_{C^0}/N_{CO} \lesssim 3$, but we would need further enhanced values, e.g., $N_{C^0}/N_{CO} \sim$ several to ~ 15 to explain the very high $R_{CI/13CO}$ observed at the AGN position of NGC 7469. However, we emphasize that the actual ratio strongly depends on the T_{ex} , which is hard to constrain by using

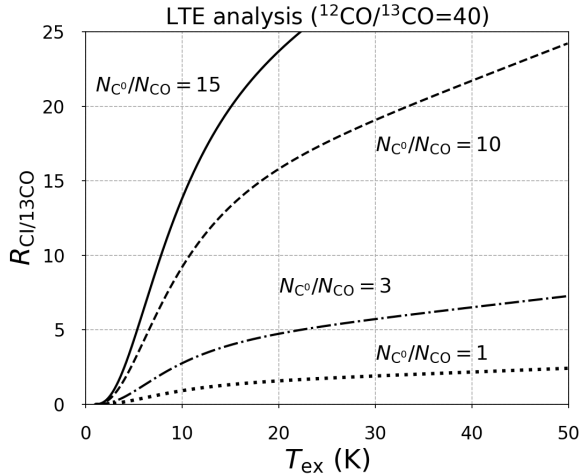


Figure 7. Expected [C I](1–0)/¹³CO(2–1) brightness temperature ratios as a function of line excitation temperature under the optically thin LTE condition. The four different curves respectively correspond to the case of $N_{C^0}/N_{CO} = 15$ (solid), = 10 (dashed), = 3 (dot-dashed), and = 1 (dotted).

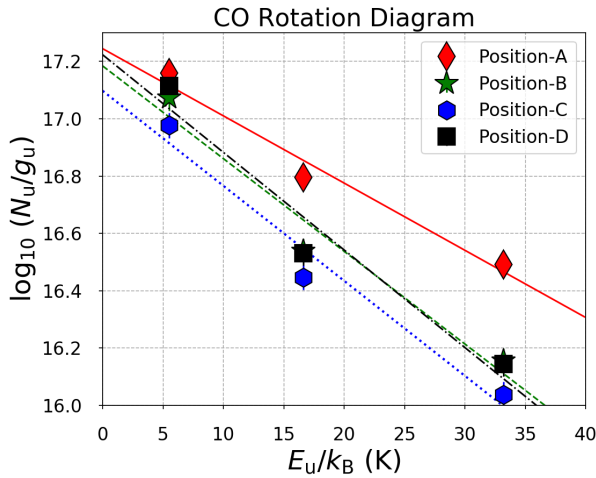


Figure 8. CO rotation diagrams of NGC 7469. The four different symbols and lines correspond to the cases at the positions A–D. The T_{ex} of each position derived from our linear regression fit are, 18.5 ± 3.2 K (A), 13.4 ± 2.9 K (B), 13.1 ± 2.5 K (C), and 12.8 ± 3.0 K (D), respectively.

the single transition [C I](1–0) line and ¹³CO(2–1) line in our hand.

On the other hand, we may roughly estimate the T_{ex} at the positions A–D by constructing rotation diagrams (Goldsmith & Langer 1999). A rotation diagram is a plot of the column density per statistical weight of a number of molecular energy levels, as a function of their energies above the ground state. From the optically thin condition, the column density of the level u (N_u) is writ-

ten as

$$N_u = \frac{8\pi k_B \nu^2 \int T_B dV}{hc^3 A_{ul}}, \quad (5)$$

where k_B and h are the Boltzmann and Planck constants, c is the speed of the light. Also, from the LTE condition, N_u can be expressed as

$$N_u = \frac{N_X}{Q(T_{\text{ex}})} g_u \exp\left(-\frac{E_u}{k_B T_{\text{ex}}}\right), \quad (6)$$

where N_X is the total column density of the given species X, $Q(T_{\text{ex}})$ is a partition function ($= \sum_u g_u \exp(-E_u/k_B T_{\text{ex}})$), and E_u is the energy at level u from the ground state. Then the logarithm of N_u/g_u vs E_u/k_B yields a straight line with a slope and the y -axis intercept indicative of T_{ex} (or rotation temperature T_{rot}) and N_X , respectively.

By using the $J = 1-0$, $2-1$, and $3-2$ CO line fluxes at the positions A–D, we constructed the rotation diagrams as shown in Figure 8. If we fit the data points by straight lines, inferred T_{ex} are 18.5 ± 3.2 K (A), 13.4 ± 2.9 K (B), 13.1 ± 2.5 K (C), and 12.8 ± 3.0 K (D), respectively. The estimated T_{ex} is relatively higher at the position-A than B–D, suggesting the existence of denser and/or warmer gas at the nucleus than at the SB ring. If these CO-based T_{ex} also hold for C⁰ and ¹³CO excitations, our prediction on N_{C^0}/N_{CO} ratios discussed above is valid. This would not be a very inappropriate speculation given the similar excitation conditions of the lines considered here (Table 2). Thus, N_{C^0}/N_{CO} is likely enhanced around the AGN as compared to the values at the SB ring.

Note that, however, the rotation temperatures derived here ought to be considered as *lower limits* of the true excitation and kinetic temperatures due to finite optical depths. Our rotation diagrams are already suggestive of this as they are obviously curved. The curved feature implies either (i) some of the lines are at least moderately optically thick and (ii) there are multiple gas components with different excitation conditions. In the case of optically thick emission (case-(i)), the N_u/g_u value of a certain transition is underestimated by a factor of $C_\tau \equiv \tau/(1 - e^{-\tau})$ (Goldsmith & Langer 1999): the actual T_{ex} critically depends on this C_τ . In order at least to cope with this optical depth effect, we need to perform non-LTE analyses.

4.1.2. Non-LTE perspective

Our non-LTE radiative transfer modelings are performed with the RADEX code (van der Tak et al. 2007) for spherical geometry to understand the underlying physical conditions of the C I-enhancement, i.e., kinetic temperature (T_{kin}), H₂ volume density (n_{H_2}), and N_X . RADEX uses an escape probability approximation to treat optical depth effects and solves statistical equilibrium in a homogeneous (i.e., single temperature and density), one-phase medium. Thus, we need to assume

that all lines observed are emitted from the same volume, although as we revealed in § 3 the real structures are quite complex. Note that we do not intend to precisely model those complex environments here. The models described below are constructed for educated guesses of the relevant parameters (see similar experiments in Izumi et al. 2016b).

In our simulation, we investigated how the following parameters affect the line ratios of our interest.

1. Kinetic temperature (T_{kin}): this affects the rate of the collisional excitation. The cases of 50, 100, 200, 300, and 500 K are investigated. This range mostly covers the CND-scale T_{kin} suggested for nearby AGNs and SB galaxies (e.g., Krips et al. 2008; Izumi et al. 2013; Viti et al. 2014).
2. Gas volume density (n_{H_2}): this also determines the rate of collisional excitation. Three cases of 10^3 , 10^4 , and 10^5 cm^{-3} are studied. These are also typical values in the CNDs of nearby galaxies (e.g., Krips et al. 2008; Izumi et al. 2013; Viti et al. 2014), as well as the values that can cover the n_{cr} of our target lines (Table 2).
3. Abundance ratio: throughout the work we assume $[\text{CO}]/[^{13}\text{CO}] = 40$ (§ 4.1.1). We studied three cases of $[\text{C}^0]/[\text{CO}] = 1.0, 3.0, \text{ and } 10.0$. Note that $[\text{C}^0]/[\text{CO}] > 1$ is required to reproduce $R_{\text{CI}/^{13}\text{CO}} > a \text{ few}$ according to Israel & Baas (2002).
4. Optical depth (τ): models with different $N_{\text{X}}/\Delta V$ are used to test this effect. Here ΔV is the line velocity width, hence the ratio $N_{\text{X}}/\Delta V$ is equivalently a ratio of a volume density of the target species to a velocity gradient over the line-of-sight. We set CO as our base species to consider this effect. For N_{CO} we made initial guesses from the observed CO fluxes. Applying the CO-to-H₂ conversion factor computed for the CND-scale of NGC 7469 (Davies et al. 2004) to the CO(1–0) fluxes in Table 7, we obtain $N_{\text{H}_2} = 1.4 \times 10^{23} \text{ cm}^{-2}$ at the position-A, as well as $N_{\text{H}_2} = (0.9\text{--}1.3) \times 10^{23} \text{ cm}^{-2}$ at the positions B–D, respectively. These translate into $N_{\text{CO}} \sim 1 \times 10^{19} \text{ cm}^{-2}$ if we assume a typical $[\text{CO}]/[\text{H}_2]$ abundance ratio of 10^{-4} . Considering this N_{CO} and the observed line widths, we here experimentally studied three cases of $N_{\text{CO}}/\Delta V = 3 \times 10^{16} \text{ cm}^{-2} (\text{km s}^{-1})^{-1}$, $1 \times 10^{17} \text{ cm}^{-2} (\text{km s}^{-1})^{-1}$, and $3 \times 10^{17} \text{ cm}^{-2} (\text{km s}^{-1})^{-1}$.
5. Background temperature (T_{bg}): this affects radiative excitation rates of the lines. While we would expect high T_{bg} particularly around an AGN, we fix this to the cosmic microwave background temperature of 2.73 K in this work for simplicity. Note that however, this parameter potentially affects

the resultant line excitation significantly, as sometimes radiative excitation becomes more important than collisional excitation (Matsushita et al. 2015; Izumi et al. 2016b). Indeed, as the upper level energy of [C I](1–0) is higher than those of CO(2–1) and $^{13}\text{CO}(2\text{--}1)$, both $R_{\text{CI}/\text{CO}}$ and $R_{\text{CI}/^{13}\text{CO}}$ would become higher when we increase T_{bg} .

The results of our radiative transfer calculations are summarized in Figure 9. It is evident that cases with higher $N_{\text{C}^0}/N_{\text{CO}}$ tend to show accordingly higher $R_{\text{CI}/\text{CO}}$ and $R_{\text{CI}/^{13}\text{CO}}$. The $R_{\text{CI}/^{13}\text{CO}}$ is highly sensitive to both T_{kin} and n_{H_2} in complex manners. In the high density cases of $n_{\text{H}_2} = 10^4$ and 10^5 cm^{-3} , the $R_{\text{CI}/^{13}\text{CO}}$ monotonically increases in higher T_{kin} . This is due to the fast reduction of $^{13}\text{CO}(2\text{--}1)$ opacity and intensity as ^{13}CO is easily excited to further upper rotational levels ($^{13}\text{CO}(2\text{--}1)$ is always very optically thin in these cases). As for the [C I](1–0), we found that its line intensity varies only slightly in each model track: although its line opacity reduces at some level, increasing T_{ex} eventually compensates the reduction to roughly maintain the resultant [C I](1–0) intensity, which leads to the enhanced $R_{\text{CI}/^{13}\text{CO}}$ in higher excitation conditions. On the other hand, the reduction of the $^{13}\text{CO}(2\text{--}1)$ opacity is only moderate in the cases of $n_{\text{H}_2} = 10^3 \text{ cm}^{-3}$. Hence $^{13}\text{CO}(2\text{--}1)$ now becomes brighter at higher T_{kin} (i.e., higher T_{ex}), which resulted in the reduction of $R_{\text{CI}/^{13}\text{CO}}$ in these low density cases. Note that [C I](1–0) is optically thin in most cases, but it can also be optically thick in limited situations, i.e., those under low excitation conditions (low n_{H_2} and low T_{kin}) with large $N_{\text{C}^0}/\Delta V \gtrsim 10^{18} \text{ cm}^{-2} (\text{km s}^{-1})^{-1}$.

The dependence of $R_{\text{CI}/\text{CO}}$ on the excitation conditions is complex as our parameter space covers both optically thick and thin regimes of CO(2–1) emission: in the cases of $n_{\text{H}_2} = 10^3$ and 10^4 cm^{-3} , $R_{\text{CI}/\text{CO}}$ tends to decrease for higher T_{kin} , as CO(2–1) intensity increases with T_{ex} in these high line opacity cases. Contrary to these, $R_{\text{CI}/\text{CO}}$ turns to increase with T_{kin} when $n_{\text{H}_2} = 10^5 \text{ cm}^{-3}$. In these latter cases the CO(2–1) intensity starts to decrease as the line now becomes optically thinner for higher T_{ex} .

Comparison of the model results in Figure 9 with the observed line ratios in Figure 6 therefore gives us an insight on the prevailing physical/chemical conditions of the C I-enhancement. We here only discuss the ratios of the SB galaxies (including the SB ring of NGC 7469) and that of the AGN of NGC 7469⁴ for simplicity. By inspecting Figure 9, it is conceivable that $N_{\text{C}^0}/N_{\text{CO}} \sim 1$ reproduces the ratios of the SB galaxies well, particularly when $T_{\text{kin}} < 100 \text{ K}$, irrespective

⁴ Both values from the double Gaussian fit and that of the channel map-basis are discussed in the same manner here.

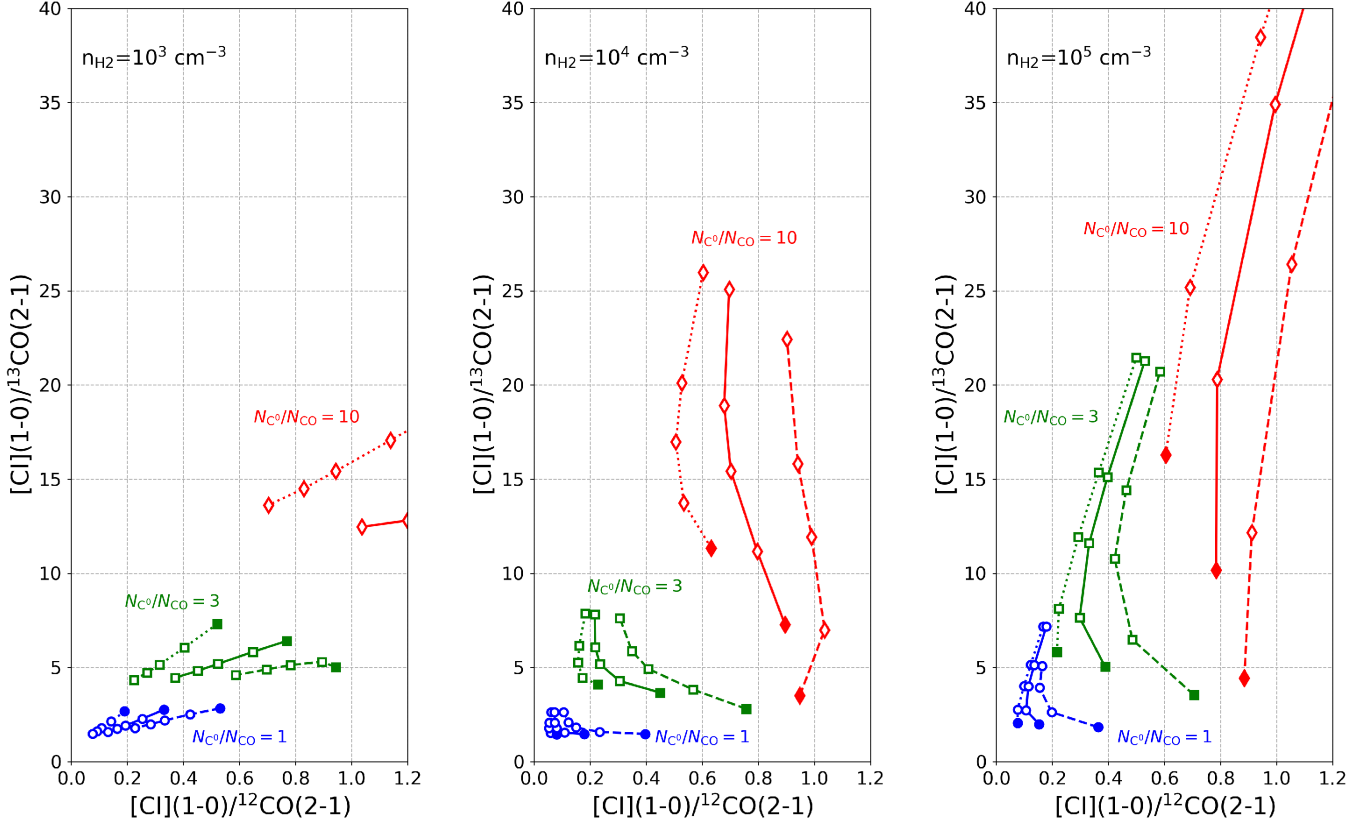


Figure 9. Radiative transfer modelings of $[C\ I](1-0)/CO(2-1)$ and $[C\ I](1-0)/^{13}CO(2-1)$ ratios (T_B unit). Three panels indicate the cases of different n_{H_2} . All model calculations assume the constant $[^{12}CO]/[^{13}CO] = 40$. In each panel, there are three groups of N_{C^0}/N_{CO} (1, 3, and 10 shown in blue, green, and red colors, respectively), where different line tracks indicate different $N_{CO}/\Delta V$: dotted = $3 \times 10^{16} \text{ cm}^{-2} (\text{km s}^{-1})^{-1}$, solid = $1 \times 10^{17} \text{ cm}^{-2} (\text{km s}^{-1})^{-1}$, and dashed = $3 \times 10^{17} \text{ cm}^{-2} (\text{km s}^{-1})^{-1}$. In each track, points indicate the five cases of T_{kin} (50, 100, 200, 300, and 500 K), with monotonically decreasing the $[C\ I](1-0)/^{13}CO(2-1)$ ratio with higher T_{kin} in the case of $n_{H_2} = 10^3 \text{ cm}^{-3}$, or conversely, monotonically increasing the $[C\ I](1-0)/^{13}CO(2-1)$ ratio with higher T_{kin} in the remaining cases, respectively: we mark the lowest $T_{\text{kin}} = 50 \text{ K}$ cases with filled symbols.

of n_{H_2} . This column density ratio (or $[C^0]/[CO]$ abundance ratio) is fully consistent with the values measured in previous works for SB galaxies (e.g., Israel & Baas 2002; Krips et al. 2016).

The interpretation of the AGN ratios is more complex, which depends on the assumed n_{H_2} . In the cases of $n_{H_2} = 10^3 \text{ cm}^{-3}$, we could not find a good solution within the parameter range we searched. This in turn suggests that the global gas density of the CNB of NGC 7469 is rather high like $\gtrsim 10^4 \text{ cm}^{-4}$. In the cases of $n_{H_2} = 10^4 \text{ cm}^{-3}$, we need both $N_{C^0}/N_{CO} \sim 10$ and $T_{\text{kin}} \gtrsim 300 - 500 \text{ K}$ to explain the observed high ratios. This abundance ratio is even $\sim 100\times$ higher than those found in the Milky Way (~ 0.1 , Oka et al. 2005), and the T_{kin} is also extremely high compared to typical values of Galactic molecular clouds ($\sim 10 \text{ K}$). In the higher n_{H_2} cases of 10^5 cm^{-3} , two possibilities arise. One is $N_{C^0}/N_{CO} \sim 3$ with high T_{kin} of $\gtrsim 300 - 500 \text{ K}$. The other is $N_{C^0}/N_{CO} \sim 10$ with a bit lower T_{kin}

of $\sim 100 - 200 \text{ K}$. In either case, it is required to elevate the $[C^0]/[CO]$ ratio by $\sim 3 - 10\times$ and the T_{kin} by $\sim 2\times - 10\times$ in the NGC 7469 AGN, as compared to the SB galaxies. Therefore, both the prevalent physical and chemical conditions are clearly different between these AGN and SB galaxies.

4.1.3. What causes the CI-enhancement?

We found that the ISM around the AGN of NGC 7469 can be characterized as that shows dramatically enhanced N_{C^0}/N_{CO} and temperature as compared to those of SB galaxies and molecular clouds in our Galaxy. As the unique point of NGC 7469 is obviously the existence of the luminous AGN, we should attribute this enhancement to the AGN, or XDR effects.

In XDRs, X-rays can ionize atoms and molecules directly deeper into the obscuring material, which can also cause doubly ionized species for heavier atoms via the Auger mechanism. The *fast electrons* produced by this

primary X-ray ionization further causes, secondary ionization, efficient gas heating due to Coulomb interaction, as well as photodissociation by internally generating UV photons. According to the prescription of Maloney et al. (1996), a key parameter to discuss XDR properties is the effective ionization parameter, which shapes gas temperature and chemical structures. It is expressed as

$$\xi_{\text{eff}} = 1.26 \times 10^{-4} \frac{F_X}{n_5 N_{22}^\phi}, \quad (7)$$

where F_X is the incident 1-100 keV flux in units of $\text{erg s}^{-1} \text{cm}^{-2}$, n_5 is the gas volume density in units of 10^5cm^{-3} , N_{22} is the attenuating column density in units of 10^{22}cm^{-2} , respectively. The parameter ϕ is related to the photon index of an X-ray SED (Γ) as $\phi = (\Gamma + 2/3)/(8/3)$. This parameter is set to 0.9 (or $\Gamma \sim 1.8$) based on actual X-ray observations of NGC 7469 (Nandra et al. 2007). With this Γ , we also estimate the 1-100 keV luminosity of NGC 7469 as $5.6 \times 10^{43} \text{erg s}^{-1}$. This X-ray luminosity is comparable to, or even larger than, the *upper limit* of the cosmic ray ($> 10^{18} \text{eV}$ proton) luminosity of NGC 7469 ($\sim 5 \times 10^{43} \text{erg s}^{-1}$ for example, for the case of the spectral index of 2.4 and the cutoff energy of $10^{20.5} \text{eV}$ for the injection cosmic ray spectrum) measured over the whole galaxy-scale (Supanitsky & de Souza 2013). Therefore, we consider that the X-rays are the prime driver of dissociation/ionization at the CN of NGC 7469.

Suppose a case of $n_5 = 1$ and $N_{22} = 10$ (typical values for CN-scale gas) for simplicity⁵, we obtain $\log \xi_{\text{eff}} \sim -2.5$ at a distance of 50 pc from the nucleus: we fully covered this area by the fixed $0''.38$ aperture. According to the one-zone dense ($n_{\text{H}_2} = 10^5 \text{cm}^{-3}$) XDR chemical model of Maloney et al. (1996), we can expect $N_{\text{CO}}/N_{\text{CO}} \sim 10$ and $T \sim 300 \text{K}$ for this ξ_{eff} , which accords well with the results of our non-LTE analysis. Note that, however, there is a drastic increase in N_{CO} , hence a correspondingly drastic decrease in $N_{\text{CO}}/N_{\text{CO}}$, toward $\log \xi_{\text{eff}} \lesssim -2.5$ according to the model. On the other hand, it is also possible that we may be overestimating the actual size of the XDR (or the region that dominantly emits [C I](1-0)) as the incident X-ray flux may be attenuated by intercepting ISM before reaching a cloud of our interest that is located away from the center. A sort of warping of the CN (e.g., Schinnerer et al. 2000) would also be potentially important as it easily alter the amount of intercepting ISM, although we do not see significant warping in the case of NGC 7469 based on our dynamical modelings (§ 4.2). In any case, it is vital to perform further higher resolution observations to map the density structure, as well as ξ_{eff} inside this CN to robustly discuss the abundance variation (see example high resolution observations to-

ward nearby AGNs to constrain these parameters in, Kawamuro et al. 2019, 2020). Even so, however, as the XDR models can at least reproduce the observed line ratios and physical/chemical conditions we unveiled, while PDR models usually do not (e.g., Hollenbach & Tielens 1999; Meijerink & Spaans 2005), we conclude that there is indeed the influence of the AGN on the surrounding ISM in the form of the XDR.

4.2. Impact on H_2 mass measurements

As the CN-scale gas of NGC 7469 is characterized by the extreme conditions described above, one would have a concern about how it impacts the H_2 mass measurements that use CO or C^0 lines. Indeed, these have been used to measure M_{H_2} (or total molecular mass M_{mol}) not only in nearby AGNs but also in high redshift quasars (e.g., Walter et al. 2011; Izumi et al. 2020), in which we certainly expect the existence of XDRs at their centers. For future high resolution observations that directly probe the CN-scale of AGNs at whichever redshift, we here try to estimate [C I](1-0)-to- or CO(1-0)-to- M_{H_2} conversion factors in NGC 7469 (CN), which will be compared with observationally- or theoretically-derived values known thus far (e.g., Bolatto et al. 2013; Offner et al. 2014; Glover et al. 2015; Jiao et al. 2017).

For this purpose, we followed the scheme of Davies et al. (2004). First, we decomposed an observed velocity field to obtain gas rotation velocity (V_{rot}) and dispersion (σ_{disp}), which determine the enclosed dynamical mass (M_{dyn}). Next, a stellar mass (M_*) profile was modeled based on high resolution *HST* maps. Then we obtained a total molecular mass as $M_{\text{mol}} = M_{\text{dyn}} - M_* - M_{\text{BH}}$, which defines CO(1-0) and [C I](1-0) conversion factors (X_{CO} and X_{CI} , respectively).

One big assumption is about the dominant phase of the circumnuclear gas in terms of mass. We here assume that H_2 still dominates the gas mass budget at the CN of NGC 7469, although we found CO and C I lines are largely affected by the XDR effects, which implies that H I (and likely H II) contribution can be significant. However, we remark that an H I column density measured by high-resolution ($0''.38$) radio absorption line observations toward the center of NGC 7469 is $N_{\text{H}} \sim 4 \times 10^{21} \text{cm}^{-2}$ (Beswick et al. 2002). This would not represent a column density toward this type-1 AGN location as the line-of-sight N_{H} measured with X-ray observations is $\sim 5 \times 10^{20} \text{cm}^{-2}$ (e.g., Kriss et al. 2000). Rather, the radio H I absorption would take place toward bright radio continuum knot(s) in the CN (i.e., close to, but not identical to the AGN itself), which are found by Very Long Baseline Interferometry (VLBI) observations (Lonsdale et al. 2003). Hence the above-mentioned N_{H} of $\sim 4 \times 10^{21} \text{cm}^{-2}$ would represent the value at the CN. This is significantly smaller than the N_{H_2} tentatively inferred from our CO(1-0) observations using, for example, the Galactic X_{CO} ($N_{\text{H}_2} \sim 1.4 \times 10^{23} \text{cm}^{-2}$; see footnote 4). Given these observational re-

⁵ Indeed, Viti et al. (2014) obtained $n_{\text{H}_2} \gtrsim 10^{4.5-5} \text{cm}^{-3}$ by modeling CO line ratios measured at the CN of NGC 1068.

sults, we provisionally assume the dominance of H_2 (or molecular gas) in the mass budget of the region of our interest. This assumption, and consequently the conversion factors derived here, should be further verified by future high resolution H I mass measurements.

In the following, we use the [C I](1–0) line and the CO(2–1) line cubes, both of which have sufficiently high S/N for dynamical modelings. Figure 10 shows the observed intensity-weighted mean velocity fields of these lines, defined as $\langle V \rangle = \Sigma_i S_i V_i / \Sigma_i S_i$ (moment 1) with 3σ clipping. The gas motion is clearly dominated by the galactic rotation with an overall northwest-southeast orientation. To extract basic beam-deconvolved dynamical information, we fitted concentric tilted rings to the data cubes by using the ^{3D}Barolo code (Di Teodoro & Fraternali 2015). The main parameters here are dynamical center, V_{rot} , σ_{disp} , radial motion (V_{rad}), V_{sys} , inclination angle (i), and position angle (PA), all of which can be varied in each ring. However, for a better convergence, we fixed the dynamical center to the AGN position. Our initial runs returned V_{sys} fully consistent with our original estimate in § 3, hence we also fixed it to 4920 km s^{-1} (optical convention): V_{rot} , σ_{disp} , V_{rad} , i , and PA are thus the major parameters to fit. For initial guesses, we set $i = 45^\circ$ and PA = 128° based on the previous CO-based dynamical work ⁶ (Davies et al. 2004). We modeled 50 concentric rings with $\Delta r = 0''.05$ starting from $r = 0''.10$. The fitting was evaluated by minimizing the residual amplitude, $|\text{model} - \text{observed data}|$.

The modeled mean velocity fields, as well as the residual images after subtracting the models from the observed images, are also shown in Figure 10. Most of the residual components are minor with $\lesssim 20 \text{ km s}^{-1}$ over the modeled region, which manifests the goodness of our fit. Figure 11 shows the radial profiles of the decomposed V_{rot} and σ_{disp} . Both lines show comparable values within $\sim 15 \text{ km s}^{-1}$ difference, suggesting that these trace essentially the same gas rotation in the currently observed regions. The variations in i and PA are very small (within 5° and 10° , respectively) around our initial guesses.

On the other hand, we found a non-negligible difference in V_{rad} : it is within $\pm 25 \text{ km s}^{-1}$ for the case of [C I](1–0) over the all radii, while it decreases down to $< -50 \text{ km s}^{-1}$ (inflow) at the innermost five rings for the case of CO(2–1). However, we claim that a significant fraction of this V_{rad} is an artifact due to the configuration of the CO(2–1) emission distribution around the center, and not due to genuinely that fast inflows. The

two bright CO(2–1) knots appear at lower and higher velocity than V_{sys} , spatially at south-west and north-east side of the AGN almost along the minor axis of this galaxy (Figure 5). Owing to this chance spatial coincidence of high- and low-velocity bright knots with the minor axis, the simple tilted-ring scheme misunderstands this configuration as that caused by fast radial flows. The real V_{rad} would be much milder such as seen in the [C I](1–0) data.

Another notable feature is an upturn in V_{rot} from $r \sim 1''.0$ to $\sim 0''.5$, which can be regarded as a sign of the Keplerian motion due to the central SMBH. Note that the sphere of influence (SOI) radius should be $\sim 3 \text{ pc}$ or $\sim 0''.01$ for the case of NGC 7469 with $M_{\text{BH}} = 1.06 \times 10^7 M_\odot$ (Peterson et al. 2014) and the stellar velocity dispersion of the bulge of $\sim 152 \text{ km s}^{-1}$ (Onken et al. 2004), which is much smaller than our beam size. However, this SOI criterion does not necessarily apply for M_{BH} measurements using gas-dynamical method as shown in previous works (e.g., Davis 2014; Nguyen et al. 2019, 2020). Further detailed dynamical modeling including the Markov Chain Monte Carlo method and the Bayesian inference to derive M_{BH} of NGC 7469 will be presented in D. Nguyen et al. (in preparation).

With the decomposed value of V_{rot} , we compute M_{dyn} as

$$\begin{aligned} M_{\text{dyn}} &= \frac{r V_{\text{rot}}^2}{G} \\ &= 230 \left(\frac{r}{\text{pc}} \right) \left(\frac{V_{\text{rot}}}{\text{km s}^{-1}} \right)^2, \end{aligned} \quad (8)$$

where G is the gravitational constant. The uncertainty of V_{rot} is typically $\sim 10\%$, which propagates to the uncertainty of M_{dyn} . The resultant M_{dyn} values are shown in Figure 12: we find very consistent values between the [C I](1–0)-based and the CO(2–1)-based M_{dyn} . The derived M_{dyn} of the concentric rings are further interpolated by a fifth-order polynomial function to estimate values at a given radius. Consequently, within $r = 0''.19$ or $\theta = 0''.38$ region where we took line ratios (§ 3.3), we find $M_{\text{dyn}} = 2.3 \times 10^8 M_\odot$ after averaging [C I](1–0)-based and CO(2–1)-based values, which has $\sim 15\%$ uncertainty.

As the next step, we used *HST* WFC3/UVIS F547M map and ACS/WFC F814W map to estimate an M_\star profile. Details of the *HST* data analysis and M_\star measurements will also be presented in D. Nguyen et al. (in preparation). The astrometry of these *HST* data were corrected by using the *Gaia* coordinates of NGC 7469. Here we used an empirical relation between the stellar continuum color and the mass-to-light ratio (M/L) developed by Bell & de Jong (2001) to measure M_\star . We assumed F547M $\sim V$ band and F814W $\sim I$ band, respectively, and applied the $(V - I)$ -to- M/L_V relation of that work. This procedure was performed in con-

⁶ Note that the Barolo code defines PA as that of the receding half of the galaxy taken anticlockwise from the north direction on the sky. We thus need to add another 180° to the observed PA (i.e., 308°), which should be put into the code. The northern part of the galaxy is the near side to us.

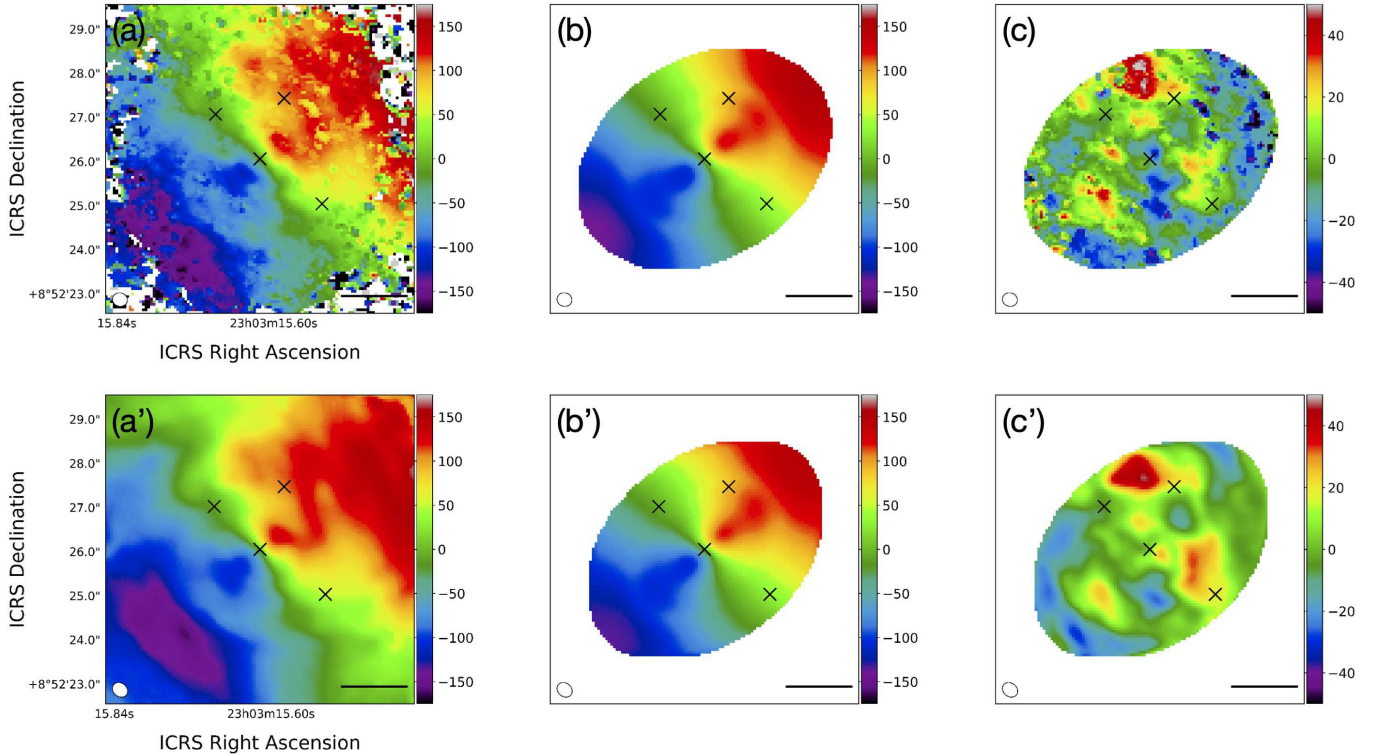


Figure 10. (a) Observed intensity-weighted mean velocity field of the [C I](1–0) emission in the central 7'' (~ 2.3 kpc) of NGC 7469. (b) Model velocity field of the [C I](1–0) by using the tilted-ring method. (c) Residual velocity image after subtracting the model from the observed map. Residuals are close to 0 km s $^{-1}$ around the AGN. (a')(b')(c') Same as the top row, but the cases for the CO(2–1) dynamics. In each panel, the four representative positions A–D (Table 6) are marked by the crosses, and the horizontal bar corresponds to 500 pc length.

centric elliptical annuli with the multiple Gaussian expansion model (MGE, [Emsellem et al. 1994](#); [Cappellari 2002](#)). The Gaussians of the MGE model are then deprojected analytically with their specific axes ratios (i.e., the ratio of the semiminor axis to the semimajor axis of each concentric elliptical Gaussian) to reconstruct a three-dimensional mass distribution and calculate the enclosed mass profile (Figure 12). Note that we masked the bright central AGN ($r \leq 0''.06$; comparable to the FWHM of the PSF of the *HST* data = $0''.08$) that saturates the F814W map at that position as well as the SB ring for our modeling. The enclosed M_* within the $r = 0''.19$ is $1.3 \times 10^8 M_\odot$. We found that the color variation is significant (~ 0.2 mag) at $r < 10''$ of NGC 7469 due likely to the complex stellar population and dust extinction, which imposes a large uncertainty on our M_* measurement as ~ 0.2 dex. This would dominate the total uncertainty in our conversion factors.

By subtracting the M_* and M_{BH} from M_{dyn} , we derive the total gas mass at $r \leq 0''.19$ as $M_{\text{mol}} = 9.5 \times 10^7 M_\odot$. The molecular hydrogen mass is $M_{\text{H}_2} = 6.7 \times 10^7 M_\odot$ for the fractional abundance of hydrogen nuclei of 71%. Note that we do not consider the contribution of dark matter here as we focus only on the very central region

of a galaxy. The CO(1–0) and [C I](1–0) line fluxes and luminosities measured over that area are, 1205 K km s $^{-1}$ and 2.3×10^7 K km s $^{-1}$ pc 2 for CO(1–0), as well as 1114 K km s $^{-1}$ and 2.1×10^7 K km s $^{-1}$ pc 2 for [C I](1–0), respectively (Table 7). Therefore, the conversion factors to the total molecular mass are, $\alpha_{\text{CO}} = 4.1 M_\odot (\text{K km s}^{-1} \text{ pc}^2)^{-1}$ and $\alpha_{\text{CI}} = 4.4 M_\odot (\text{K km s}^{-1} \text{ pc}^2)^{-1}$, respectively. The corresponding factors for N_{H_2} measurements are, $X_{\text{CO}} = 1.9 \times 10^{20} \text{ cm}^{-2} (\text{K km s}^{-1})^{-1}$ and $X_{\text{CI}} = 2.1 \times 10^{20} \text{ cm}^{-2} (\text{K km s}^{-1})^{-1}$, respectively. The uncertainties of M_{dyn} measurement and M_* measurements jointly yield the uncertainties of these factors, which are then ~ 0.3 dex, although it is hard to constrain this number accurately.

Our X_{CO} is very comparable to the canonical Milky Way value ([Bolatto et al. 2013](#); [Offner et al. 2014](#)). It is $\sim 3\times$ larger than the typical value inferred for AGNs based on kpc-scale resolution observations (e.g., [Sandstrom et al. 2013](#)), and is also $1.6\times$ larger than the X_{CO} previously measured for NGC 7469 itself over the central ~ 1.7 kpc region ([Davies et al. 2004](#)). A smaller X_{CO} than the Milky Way value has been observed in nuclear regions of normal spiral galaxies as well, likely due to tidal effects on molecular clouds ([Meier & Turner](#)

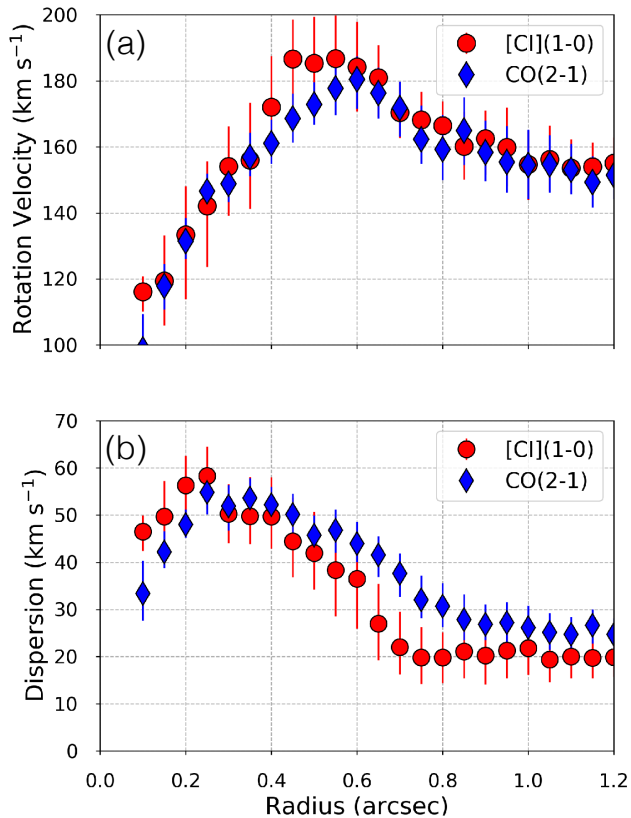


Figure 11. Radial profiles of the beam-deconvolved (a) rotation velocity (V_{rot}) and (b) velocity dispersion (σ_{disp}) at the innermost $r < 1''.2$. The cases of the [C I](1–0) (red circles) and the CO(2–1) (blue diamonds) dynamics are displayed.

2004; Meier et al. 2008). Hence, our X_{CO} seems contradictory to the previously reported trend of decreasing X_{CO} toward more active environments including AGNs. This is due to the high spatial resolution of this work that allows us to probe the XDR (i.e., the region at which CO molecules are dissociated to some level) of NGC 7469 properly, which should result in a large X_{CO} for a given H_2 mass. If this is the case, the consistency of our X_{CO} to the Milky Way value is simply a chance coincidence, as the underlying physical/chemical conditions must be different greatly. It is noteworthy in this context that our relatively large X_{CO} is consistent with the value reported by Wada et al. (2018), who simulated CND-scale CO properties around an AGN by incorporating the XDR chemical network of Meijerink & Spaans (2005). However, Wada et al. (2018) also claimed that there can be a quite large dispersion in X_{CO} up to one order of magnitude. Therefore, similar high resolution observations toward a statistical number of AGNs are required to assess X_{CO} and its scatter at their close vicinities.

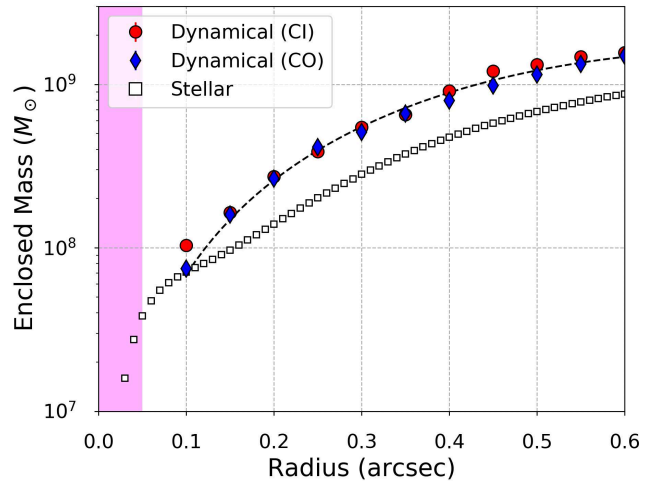


Figure 12. Enclosed stellar mass (M_*) and dynamical mass (M_{dyn} ; based on the [C I](1–0) dynamics or CO(2–1) dynamics) around the center of NGC 7469. The M_* values are returned from the MGE model (see details in D. Nguyen et al. in preparation), by using the high resolution *HST* WFC3/UVIS F547M and ACS/WFC F814W maps with the color– M/L_V relation (Bell & de Jong 2001). The region masked out for the M_* measurement is shaded ($r < 0''.06$). Our tentative fit for the M_{dyn} profile by using a 5th order polynomial function is shown by the dashed line.

Our C^0 conversion factors (α_{CI} and X_{CI}) are $\sim 5\times$ smaller than the values expected for Galactic star-forming clouds (Offner et al. 2014; Glover et al. 2015). Jiao et al. (2017) estimated $\alpha_{\text{CI}} = 7.6 M_{\odot} (\text{K km s}^{-1} \text{pc}^2)^{-1}$ for a sample of 71 nearby U/LIRGs based on *Herschel* observations. Our conversion factors are still $\sim 2\times$ smaller than this value, as well as than that individually derived for another ULIRG NGC 6240 (Cicone et al. 2018). The observational estimation of X_{CI} critically depends on the inverse of the C^0 relative abundance to H_2 : for example Jiao et al. (2017) assumed $[\text{C}^0]/[\text{H}_2] = 3 \times 10^{-5}$, which is a value of the $z = 2.5$ Cloverleaf quasar estimated over its galaxy-scale (Weiß et al. 2003). If the $[\text{C}^0]/[\text{H}_2]$ value for the central ~ 100 pc region of NGC 7469 is larger than the values of our Galactic star-forming clouds and those of U/LIRGs, our smaller conversion factors are understandable. This is again very likely the case as we now probe the XDR of NGC 7469, where we can expect a ratio as high as $\gtrsim 10^{-4}$ according to XDR models (e.g., Maloney et al. 1996).

As our method to estimate the conversion factors is rather direct, they would be useful to estimate M_{H_2} at the vicinities of AGNs. However, as the nature of an XDR is dependent on several physical parameters including X-ray luminosity, gas density, and attenuating column density, similar efforts to what we have per-

formed here are highly required to obtain characteristic conversion factors, if exist, and to assess their scatter.

5. SUMMARY

In this paper we present high resolution (~ 130 pc) ALMA observations of multiple CO and C⁰ lines toward the central kpc region of the luminous type-1 Seyfert galaxy NGC 7469. The region consists of the CND (central $\sim 1''$) and the surrounding SB ring (radius $\sim 1''.5$). All of the targeted emission lines, namely CO(1–0), CO(2–1), CO(3–2), ¹³CO(2–1), and [C I](1–0), are successfully detected both in the CND and the SB ring. Thanks to the high resolution, we could reliably measure the line fluxes and their ratios, which are used to discuss the nature of ISM particularly at the vicinity of the AGN in a context of X-ray dominated region (XDR) chemistry. Our findings of this work are summarized in the following.

1. ¹²CO lines are bright both at the CND and the SB ring, which defines the base gas distribution of this galaxy. On the other hand, ¹³CO(2–1) is very faint at the CND, while [C I](1–0) emission is concentrated toward the CND. The [C I](1–0) emission distribution clearly peaks at the exact AGN position, whereas CO and ¹³CO distributions do not. This is unlikely due to absorption effect considering the type-1 Seyfert geometry, and already hints at the influence of the AGN on the gas physical/chemical structures. Given the centrally-peaked distribution, the [C I](1–0) emission also defines the systemic velocity of this galaxy as $V_{\text{sys}} = 4920$ km s^{–1}.
2. Consequently, we found the line flux ratios of [C I](1–0)/CO(2–1) ($\equiv R_{\text{CI/CO}}$) and [C I](1–0)/¹³CO(2–1) ($\equiv R_{\text{CI/13CO}}$), measured over ~ 130 pc area, are dramatically different between the CND and the SB ring (i.e., C I-enhancement in the CND). There is a trend of increasing these ratios in AGNs as compared to SB galaxies or quiescent galaxies as found in the compilation of the single dish-based data. But the ratios we revealed at the CND of NGC 7469 are extraordinary ($R_{\text{CI/CO}} \sim 0.5$ and $R_{\text{CI/13CO}} \sim 20$ as integrated flux ratios, or $R_{\text{CI/CO}} \sim 0.8$ and $R_{\text{CI/13CO}} \sim 25$ as channel map-based ratios), which have never been observed at the spatial scales probed here: these AGN ratios are $\sim 3\times$ and $\sim 10\times$ higher than typical values of SB galaxies.
3. The high ratios observed at the CND indicate the power of the high resolution provided by ALMA, which allows us to selectively probe the regions influenced by the AGN (or likely XDR). We suggest that these ratios would have a potential as a submm diagnostic method of the underlying heating sources (AGN vs SB).
4. Our LTE and non-LTE analysis of the line ratios both indicate that we need an elevated C⁰/CO abundance ratio around the AGN as compared to that of the SB ring of this galaxy, likely by $\sim 3 - 10\times$, to reproduce the different line ratios observed. Moreover, we need a higher gas kinetic temperature ($\sim 100 - 500$ K) as well around the AGN than those at the SB ring (< 100 K). Note that within the parameter range studied here, both [C I](1–0) and ¹³CO(2–1) lines are optically thin in most cases.
5. The unique abundance ratios and high gas temperature are well in accord with the scenario that the AGN influences the surrounding physical and chemical structures of the ISM in the form of XDR.
6. We modeled the velocity fields of the [C I](1–0) line and the CO(2–1) line cubes by using a tilted-ring method. We found consistent rotation velocity (V_{rot}) and dispersion (σ_{disp}) between these two lines. Using the V_{rot} , we could measure enclosed dynamical mass (M_{dyn}) inside a given radius. For example, M_{dyn} at $r \leq 0''.19$ (~ 60 pc) is $2.3 \times 10^8 M_{\odot}$.
7. As we revealed unusual ISM conditions around the AGN of NGC 7469, we computed dedicated conversion factors from CO(1–0) and [C I](1–0) luminosities to the total molecular (or H₂) mass by also using the results of our dynamical modelings. Our big assumption is the dominance of H₂ gas over the gas mass budget at the innermost ~ 100 pc region of NGC 7469. We obtained $\alpha_{\text{CO}} = 4.1 M_{\odot} (\text{K km s}^{-1} \text{ pc}^2)^{-1}$ and $\alpha_{\text{CI}} = 4.4 M_{\odot} (\text{K km s}^{-1} \text{ pc}^2)^{-1}$ for the central ~ 100 pc of NGC 7469. Alternatively $X_{\text{CO}} = 1.9 \times 10^{20} \text{ cm}^{-2} (\text{K km s}^{-1})^{-1}$ and $X_{\text{CI}} = 2.1 \times 10^{20} \text{ cm}^{-2} (\text{K km s}^{-1})^{-1}$. The [C I](1–0) conversion factors of NGC 7469 are smaller than those derived for Galactic star-forming regions and for nearby U/LIRGs, which would be a natural consequence of elevated C⁰ abundance in the XDR of NGC 7469.

The C I-enhancement captured in this work is a quite dramatic phenomenon. As it is only based on the results of NGC 7469, we will further investigate the trend by increasing the sample galaxies, and will extensively discuss the ISM properties by also comparing the ratios with state-of-the-art chemical models. For the particular case of NGC 7469, we guide readers to our forthcoming paper (S. Nakano et al. in preparation) for such comparisons. If the trend is confirmed, the C I-enhancement will be used as a submm energy diagnostic method that is applicable to dusty environments as this wavelength does not suffer from severe dust extinction (except for some very extremely dusty cases seen in so-called compact obscured nuclei = CONs, e.g., Sakamoto et al. 2013;

Aalto et al. 2019), as well as to high redshift galaxies owing to the high ν_{rest} of [C I](1–0).

ACKNOWLEDGMENTS

We thank the anonymous referee for her/his thorough reading and very constructive feedback, which improved this work greatly. This paper makes use of the following ALMA data: ADS/JAO.ALMA#2017.1.00078.S. ALMA is a partnership of ESO (representing its member states), NSF (USA) and NINS (Japan), together with NRC (Canada), MOST and ASIAA (Taiwan), and KASI (Republic of Korea), in cooperation with the Republic of Chile. The Joint ALMA Observatory is operated by ESO, AUI/NRAO and NAOJ. We used data based on observations with the NASA/ESA *Hubble Space Telescope* and obtained from the Hubble Legacy Archive, which is a collaboration between the Space Telescope Science Institute (STScI/NASA), the Space Telescope European Coordinating Facility (ST-ECF/ESA), and the Canadian Astronomy Data Centre (CADM/NRC/CSA). T.I., S.B, T.K. and K.K are supported by Japan Society for the Promotion of Science (JSPS) KAKENHI Grant Number JP20K14531, 19J00892, JP20K14529, and JP17H06130, respectively. K.K. is also supported by the NAOJ ALMA Scientific Research Grant Number 2017-06B. T.I. was supported by the ALMA Japan Research Grant of NAOJ ALMA Project, NAOJ-ALMA-241.

REFERENCES

- Aalto, S., Black, J. H., Johansson, L. E. B., & Booth, R. S. 1991, *A&A*, 249, 323
- Aalto, S., Booth, R. S., Black, J. H., & Johansson, L. E. B. 1995, *A&A*, 300, 369
- Aalto, S., Muller, S., König, S., et al. 2019, *A&A*, 627, A147, doi: [10.1051/0004-6361/201935480](https://doi.org/10.1051/0004-6361/201935480)
- Alaghband-Zadeh, S., Chapman, S. C., Swinbank, A. M., et al. 2013, *MNRAS*, 435, 1493, doi: [10.1093/mnras/stt1390](https://doi.org/10.1093/mnras/stt1390)
- Bell, E. F., & de Jong, R. S. 2001, *ApJ*, 550, 212, doi: [10.1086/319728](https://doi.org/10.1086/319728)
- Beswick, R. J., Pedlar, A., & McDonald, A. R. 2002, *MNRAS*, 335, 1091, doi: [10.1046/j.1365-8711.2002.05699.x](https://doi.org/10.1046/j.1365-8711.2002.05699.x)
- Blustin, A. J., Kriss, G. A., Holczer, T., et al. 2007, *A&A*, 466, 107, doi: [10.1051/0004-6361:20066883](https://doi.org/10.1051/0004-6361:20066883)
- Bolatto, A. D., Wolfire, M., & Leroy, A. K. 2013, *ARA&A*, 51, 207, doi: [10.1146/annurev-astro-082812-140944](https://doi.org/10.1146/annurev-astro-082812-140944)
- Bothwell, M. S., Aguirre, J. E., Aravena, M., et al. 2017, *MNRAS*, 466, 2825, doi: [10.1093/mnras/stw3270](https://doi.org/10.1093/mnras/stw3270)
- Buchner, J., Georgakakis, A., Nandra, K., et al. 2015, *ApJ*, 802, 89, doi: [10.1088/0004-637X/802/2/89](https://doi.org/10.1088/0004-637X/802/2/89)
- Cappellari, M. 2002, *MNRAS*, 333, 400, doi: [10.1046/j.1365-8711.2002.05412.x](https://doi.org/10.1046/j.1365-8711.2002.05412.x)
- Cazzoli, S., Gil de Paz, A., Márquez, I., et al. 2020, *MNRAS*, 493, 3656, doi: [10.1093/mnras/staa409](https://doi.org/10.1093/mnras/staa409)
- Cicone, C., Severgnini, P., Papadopoulos, P. P., et al. 2018, *ApJ*, 863, 143, doi: [10.3847/1538-4357/aad32a](https://doi.org/10.3847/1538-4357/aad32a)
- Colina, L., Díaz-Santos, T., Alonso-Herrero, A., et al. 2007, *A&A*, 467, 559, doi: [10.1051/0004-6361:20067043](https://doi.org/10.1051/0004-6361:20067043)
- Condon, J. J., Huang, Z. P., Yin, Q. F., & Thuan, T. X. 1991, *ApJ*, 378, 65, doi: [10.1086/170407](https://doi.org/10.1086/170407)
- Costagliola, F., Aalto, S., Rodriguez, M. I., et al. 2011, *A&A*, 528, A30, doi: [10.1051/0004-6361/201015628](https://doi.org/10.1051/0004-6361/201015628)
- Crocker, A. F., Pellegrini, E., Smith, J. D. T., et al. 2019, *ApJ*, 887, 105, doi: [10.3847/1538-4357/ab4196](https://doi.org/10.3847/1538-4357/ab4196)
- Davies, R. I., Müller Sánchez, F., Genzel, R., et al. 2007, *ApJ*, 671, 1388, doi: [10.1086/523032](https://doi.org/10.1086/523032)
- Davies, R. I., Tacconi, L. J., & Genzel, R. 2004, *ApJ*, 602, 148, doi: [10.1086/380995](https://doi.org/10.1086/380995)

- Davis, T. A. 2014, *MNRAS*, 443, 911, doi: [10.1093/mnras/stu1163](https://doi.org/10.1093/mnras/stu1163)
- de Vaucouleurs, G., de Vaucouleurs, A., Corwin, Herold G., J., et al. 1991, *Third Reference Catalogue of Bright Galaxies*
- Di Teodoro, E. M., & Fraternali, F. 2015, *MNRAS*, 451, 3021, doi: [10.1093/mnras/stv1213](https://doi.org/10.1093/mnras/stv1213)
- Díaz, A. I., Álvarez, M. Á., Terlevich, E., et al. 2000, *MNRAS*, 311, 120, doi: [10.1046/j.1365-8711.2000.03020.x](https://doi.org/10.1046/j.1365-8711.2000.03020.x)
- Díaz-Santos, T., Alonso-Herrero, A., Colina, L., Ryder, S. D., & Knapen, J. H. 2007, *ApJ*, 661, 149, doi: [10.1086/513089](https://doi.org/10.1086/513089)
- Emsellem, E., Monnet, G., & Bacon, R. 1994, *A&A*, 285, 723
- Esquej, P., Alonso-Herrero, A., González-Martín, O., et al. 2014, *ApJ*, 780, 86, doi: [10.1088/0004-637X/780/1/86](https://doi.org/10.1088/0004-637X/780/1/86)
- Fathi, K., Izumi, T., Romeo, A. B., et al. 2015, *ApJL*, 806, L34, doi: [10.1088/2041-8205/806/2/L34](https://doi.org/10.1088/2041-8205/806/2/L34)
- García-Burillo, S., Combes, F., Usero, A., et al. 2014, *A&A*, 567, A125, doi: [10.1051/0004-6361/201423843](https://doi.org/10.1051/0004-6361/201423843)
- Genzel, R., Weitzel, L., Tacconi-Garman, L. E., et al. 1995, *ApJ*, 444, 129, doi: [10.1086/175588](https://doi.org/10.1086/175588)
- Gerin, M., & Phillips, T. G. 2000, *ApJ*, 537, 644, doi: [10.1086/309072](https://doi.org/10.1086/309072)
- Glover, S. C. O., Clark, P. C., Micic, M., & Molina, F. 2015, *MNRAS*, 448, 1607, doi: [10.1093/mnras/stu2699](https://doi.org/10.1093/mnras/stu2699)
- Goldsmith, P. F., & Langer, W. D. 1999, *ApJ*, 517, 209, doi: [10.1086/307195](https://doi.org/10.1086/307195)
- Guesten, R., Henkel, C., & Batrla, W. 1985, *A&A*, 149, 195
- Harada, N., Herbst, E., & Wakelam, V. 2010, *ApJ*, 721, 1570, doi: [10.1088/0004-637X/721/2/1570](https://doi.org/10.1088/0004-637X/721/2/1570)
- Harada, N., Thompson, T. A., & Herbst, E. 2013, *ApJ*, 765, 108, doi: [10.1088/0004-637X/765/2/108](https://doi.org/10.1088/0004-637X/765/2/108)
- Heintz, K. E., & Watson, D. 2020, *ApJL*, 889, L7, doi: [10.3847/2041-8213/ab6733](https://doi.org/10.3847/2041-8213/ab6733)
- Henkel, C., Chin, Y. N., Mauersberger, R., & Whiteoak, J. B. 1998, *A&A*, 329, 443, <https://arxiv.org/abs/astro-ph/9710254>
- Henkel, C., Asiri, H., Ao, Y., et al. 2014, *A&A*, 565, A3, doi: [10.1051/0004-6361/201322962](https://doi.org/10.1051/0004-6361/201322962)
- Hickox, R. C., & Alexander, D. M. 2018, *ARA&A*, 56, 625, doi: [10.1146/annurev-astro-081817-051803](https://doi.org/10.1146/annurev-astro-081817-051803)
- Hollenbach, D. J., & Tielens, A. G. G. M. 1997, *ARA&A*, 35, 179, doi: [10.1146/annurev.astro.35.1.179](https://doi.org/10.1146/annurev.astro.35.1.179)
- . 1999, *Reviews of Modern Physics*, 71, 173, doi: [10.1103/RevModPhys.71.173](https://doi.org/10.1103/RevModPhys.71.173)
- Ikeda, M., Oka, T., Tatematsu, K., Sekimoto, Y., & Yamamoto, S. 2002, *ApJS*, 139, 467, doi: [10.1086/338761](https://doi.org/10.1086/338761)
- Ikeda, M., Maezawa, H., Ito, T., et al. 1999, *ApJL*, 527, L59, doi: [10.1086/312395](https://doi.org/10.1086/312395)
- Imanishi, M., Nakanishi, K., & Izumi, T. 2016, *AJ*, 152, 218, doi: [10.3847/0004-6256/152/6/218](https://doi.org/10.3847/0004-6256/152/6/218)
- Imanishi, M., Nakanishi, K., Tamura, Y., Oi, N., & Kohno, K. 2007, *AJ*, 134, 2366, doi: [10.1086/523598](https://doi.org/10.1086/523598)
- Imanishi, M., & Wada, K. 2004, *ApJ*, 617, 214, doi: [10.1086/425245](https://doi.org/10.1086/425245)
- Israel, F. P., & Baas, F. 2002, *A&A*, 383, 82, doi: [10.1051/0004-6361:20011736](https://doi.org/10.1051/0004-6361:20011736)
- Israel, F. P., Rosenberg, M. J. F., & van der Werf, P. 2015, *A&A*, 578, A95, doi: [10.1051/0004-6361/201425175](https://doi.org/10.1051/0004-6361/201425175)
- Izumi, T., Kawakatu, N., & Kohno, K. 2016a, *ApJ*, 827, 81, doi: [10.3847/0004-637X/827/1/81](https://doi.org/10.3847/0004-637X/827/1/81)
- Izumi, T., Wada, K., Fukushige, R., Hamamura, S., & Kohno, K. 2018, *ApJ*, 867, 48, doi: [10.3847/1538-4357/aae20b](https://doi.org/10.3847/1538-4357/aae20b)
- Izumi, T., Kohno, K., Martín, S., et al. 2013, *PASJ*, 65, 100, doi: [10.1093/pasj/65.5.100](https://doi.org/10.1093/pasj/65.5.100)
- Izumi, T., Kohno, K., Aalto, S., et al. 2015, *ApJ*, 811, 39, doi: [10.1088/0004-637X/811/1/39](https://doi.org/10.1088/0004-637X/811/1/39)
- . 2016b, *ApJ*, 818, 42, doi: [10.3847/0004-637X/818/1/42](https://doi.org/10.3847/0004-637X/818/1/42)
- Izumi, T., Silverman, J. D., Jahnke, K., et al. 2020, *arXiv e-prints*, arXiv:2006.03072, <https://arxiv.org/abs/2006.03072>
- Jiao, Q., Zhao, Y., Zhu, M., et al. 2017, *ApJL*, 840, L18, doi: [10.3847/2041-8213/aa6f0f](https://doi.org/10.3847/2041-8213/aa6f0f)
- Jiao, Q., Zhao, Y., Lu, N., et al. 2019, *ApJ*, 880, 133, doi: [10.3847/1538-4357/ab29ed](https://doi.org/10.3847/1538-4357/ab29ed)
- Kamenetzky, J., Glenn, J., Rangwala, N., et al. 2012, *ApJ*, 753, 70, doi: [10.1088/0004-637X/753/1/70](https://doi.org/10.1088/0004-637X/753/1/70)
- Kawamuro, T., Izumi, T., & Imanishi, M. 2019, *PASJ*, 71, 68, doi: [10.1093/pasj/psz045](https://doi.org/10.1093/pasj/psz045)
- Kawamuro, T., Izumi, T., Onishi, K., et al. 2020, *ApJ*, 895, 135, doi: [10.3847/1538-4357/ab8b62](https://doi.org/10.3847/1538-4357/ab8b62)
- Kazandjian, M. V., Meijerink, R., Pelupessy, I., Israel, F. P., & Spaans, M. 2012, *A&A*, 542, A65, doi: [10.1051/0004-6361/201118641](https://doi.org/10.1051/0004-6361/201118641)
- . 2015, *A&A*, 574, A127, doi: [10.1051/0004-6361/201322805](https://doi.org/10.1051/0004-6361/201322805)
- Keene, J., Lis, D. C., Phillips, T. G., & Schilke, P. 1997, in *IAU Symposium*, Vol. 178, *IAU Symposium*, ed. E. F. van Dishoeck, 129–139
- Kohno, K. 2005, in *American Institute of Physics Conference Series*, Vol. 783, *The Evolution of Starbursts*, ed. S. Hüttmeister, E. Manthey, D. Bomans, & K. Weis, 203–208, doi: [10.1063/1.2034987](https://doi.org/10.1063/1.2034987)
- Kohno, K., Matsushita, S., Vila-Vilaró, B., et al. 2001, *Astronomical Society of the Pacific Conference Series*, Vol. 249, *Dense Molecular Gas and Star Formation in Nearby Seyfert Galaxies*, ed. J. H. Knapen, J. E. Beckman, I. Shlosman, & T. J. Mahoney, 672

- Krips, M., Neri, R., García-Burillo, S., et al. 2008, *ApJ*, 677, 262, doi: [10.1086/527367](https://doi.org/10.1086/527367)
- Krips, M., Martín, S., Sakamoto, K., et al. 2016, *A&A*, 592, L3, doi: [10.1051/0004-6361/201628882](https://doi.org/10.1051/0004-6361/201628882)
- Kriss, G. A., Peterson, B. M., Crenshaw, D. M., & Zheng, W. 2000, *ApJ*, 535, 58, doi: [10.1086/308840](https://doi.org/10.1086/308840)
- Langer, W. D., Graedel, T. E., Frerking, M. A., & Armentrout, P. B. 1984, *ApJ*, 277, 581, doi: [10.1086/161730](https://doi.org/10.1086/161730)
- Lepp, S., & Dalgarno, A. 1996, *A&A*, 306, L21
- Leroy, A. K., Walter, F., Brinks, E., et al. 2008, *AJ*, 136, 2782, doi: [10.1088/0004-6256/136/6/2782](https://doi.org/10.1088/0004-6256/136/6/2782)
- Leroy, A. K., Walter, F., Sandstrom, K., et al. 2013, *AJ*, 146, 19, doi: [10.1088/0004-6256/146/2/19](https://doi.org/10.1088/0004-6256/146/2/19)
- Liu, T., Wang, J.-X., Yang, H., Zhu, F.-F., & Zhou, Y.-Y. 2014, *ApJ*, 783, 106, doi: [10.1088/0004-637X/783/2/106](https://doi.org/10.1088/0004-637X/783/2/106)
- Lonsdale, C. J., Lonsdale, C. J., Smith, H. E., & Diamond, P. J. 2003, *ApJ*, 592, 804, doi: [10.1086/375778](https://doi.org/10.1086/375778)
- Lucas, R., & Liszt, H. 1998, *A&A*, 337, 246
- Malkan, M. A., Gorjian, V., & Tam, R. 1998, *ApJS*, 117, 25, doi: [10.1086/313110](https://doi.org/10.1086/313110)
- Maloney, P. R., Hollenbach, D. J., & Tielens, A. G. G. M. 1996, *ApJ*, 466, 561, doi: [10.1086/177532](https://doi.org/10.1086/177532)
- Martín, S., Aladro, R., Martín-Pintado, J., & Mauersberger, R. 2010, *A&A*, 522, A62, doi: [10.1051/0004-6361/201014972](https://doi.org/10.1051/0004-6361/201014972)
- Martín, S., Muller, S., Henkel, C., et al. 2019, *A&A*, 624, A125, doi: [10.1051/0004-6361/201935106](https://doi.org/10.1051/0004-6361/201935106)
- Mateo, M. L. 1998, *ARA&A*, 36, 435, doi: [10.1146/annurev.astro.36.1.435](https://doi.org/10.1146/annurev.astro.36.1.435)
- Matsushita, S., Kohno, K., Vila-Vilaro, B., Tosaki, T., & Kawabe, R. 1998, *ApJ*, 495, 267, doi: [10.1086/305261](https://doi.org/10.1086/305261)
- Matsushita, S., Trung, D.-V., Boone, F., et al. 2015, *ApJ*, 799, 26, doi: [10.1088/0004-637X/799/1/26](https://doi.org/10.1088/0004-637X/799/1/26)
- McMullin, J. P., Waters, B., Schiebel, D., Young, W., & Golap, K. 2007, *Astronomical Society of the Pacific Conference Series*, Vol. 376, *CASA Architecture and Applications*, ed. R. A. Shaw, F. Hill, & D. J. Bell (San Francisco, CA: ASP), 127
- Meier, D. S., & Turner, J. L. 2004, *AJ*, 127, 2069, doi: [10.1086/382904](https://doi.org/10.1086/382904)
- Meier, D. S., Turner, J. L., & Hurt, R. L. 2008, *ApJ*, 675, 281, doi: [10.1086/524932](https://doi.org/10.1086/524932)
- Meijerink, R., & Spaans, M. 2005, *A&A*, 436, 397, doi: [10.1051/0004-6361:20042398](https://doi.org/10.1051/0004-6361:20042398)
- Meijerink, R., Spaans, M., & Israel, F. P. 2007, *A&A*, 461, 793, doi: [10.1051/0004-6361:20066130](https://doi.org/10.1051/0004-6361:20066130)
- Meijerink, R., Spaans, M., Loenen, A. F., & van der Werf, P. P. 2011, *A&A*, 525, A119, doi: [10.1051/0004-6361/201015136](https://doi.org/10.1051/0004-6361/201015136)
- Meixner, M., Puchalsky, R., Blitz, L., Wright, M., & Heckman, T. 1990, *ApJ*, 354, 158, doi: [10.1086/168675](https://doi.org/10.1086/168675)
- Meixner, M., & Tielens, A. G. G. M. 1993, *ApJ*, 405, 216, doi: [10.1086/172355](https://doi.org/10.1086/172355)
- Milam, S. N., Savage, C., Brewster, M. A., Ziurys, L. M., & Wyckoff, S. 2005, *ApJ*, 634, 1126, doi: [10.1086/497123](https://doi.org/10.1086/497123)
- Miyamoto, Y., Seta, M., Nakai, N., et al. 2018, *PASJ*, 70, L1, doi: [10.1093/pasj/psy016](https://doi.org/10.1093/pasj/psy016)
- Nandra, K., Le, T., George, I. M., et al. 2000, *ApJ*, 544, 734, doi: [10.1086/317237](https://doi.org/10.1086/317237)
- Nandra, K., O'Neill, P. M., George, I. M., & Reeves, J. N. 2007, *MNRAS*, 382, 194, doi: [10.1111/j.1365-2966.2007.12331.x](https://doi.org/10.1111/j.1365-2966.2007.12331.x)
- Nesvadba, N. P. H., Cañameras, R., Kneissl, R., et al. 2019, *A&A*, 624, A23, doi: [10.1051/0004-6361/201833777](https://doi.org/10.1051/0004-6361/201833777)
- Nguyen, D. D., Seth, A. C., Neumayer, N., et al. 2019, *ApJ*, 872, 104, doi: [10.3847/1538-4357/aafe7a](https://doi.org/10.3847/1538-4357/aafe7a)
- Nguyen, D. D., den Brok, M., Seth, A. C., et al. 2020, *ApJ*, 892, 68, doi: [10.3847/1538-4357/ab77aa](https://doi.org/10.3847/1538-4357/ab77aa)
- Offner, S. S. R., Bisbas, T. G., Bell, T. A., & Viti, S. 2014, *MNRAS*, 440, L81, doi: [10.1093/mnrasl/slu013](https://doi.org/10.1093/mnrasl/slu013)
- Ojha, R., Stark, A. A., Hsieh, H. H., et al. 2001, *ApJ*, 548, 253, doi: [10.1086/318693](https://doi.org/10.1086/318693)
- Oka, T., Kamegai, K., Hayashida, M., et al. 2005, *ApJ*, 623, 889, doi: [10.1086/428707](https://doi.org/10.1086/428707)
- Okada, Y., Güsten, R., Requena-Torres, M. A., et al. 2019, *A&A*, 621, A62, doi: [10.1051/0004-6361/201833398](https://doi.org/10.1051/0004-6361/201833398)
- Onken, C. A., Ferrarese, L., Merritt, D., et al. 2004, *ApJ*, 615, 645, doi: [10.1086/424655](https://doi.org/10.1086/424655)
- Orienti, M., & Prieto, M. A. 2010, *MNRAS*, 401, 2599, doi: [10.1111/j.1365-2966.2009.15837.x](https://doi.org/10.1111/j.1365-2966.2009.15837.x)
- Osterbrock, D. E., & Martel, A. 1993, *ApJ*, 414, 552, doi: [10.1086/173102](https://doi.org/10.1086/173102)
- Papadopoulos, P. P., & Allen, M. L. 2000, *ApJ*, 537, 631, doi: [10.1086/309066](https://doi.org/10.1086/309066)
- Papadopoulos, P. P., Bisbas, T. G., & Zhang, Z.-Y. 2018, *MNRAS*, 478, 1716, doi: [10.1093/mnras/sty1077](https://doi.org/10.1093/mnras/sty1077)
- Papadopoulos, P. P., & Greve, T. R. 2004, *ApJL*, 615, L29, doi: [10.1086/426059](https://doi.org/10.1086/426059)
- Papadopoulos, P. P., Thi, W. F., & Viti, S. 2004, *MNRAS*, 351, 147, doi: [10.1111/j.1365-2966.2004.07762.x](https://doi.org/10.1111/j.1365-2966.2004.07762.x)
- Pereira-Santaella, M., Alonso-Herrero, A., Santos-Lleo, M., et al. 2011, *A&A*, 535, A93, doi: [10.1051/0004-6361/201117420](https://doi.org/10.1051/0004-6361/201117420)
- Peterson, B. M., Grier, C. J., Horne, K., et al. 2014, *ApJ*, 795, 149, doi: [10.1088/0004-637X/795/2/149](https://doi.org/10.1088/0004-637X/795/2/149)
- Petrucchi, P. O., Maraschi, L., Haardt, F., & Nandra, K. 2004, *A&A*, 413, 477, doi: [10.1051/0004-6361:20031499](https://doi.org/10.1051/0004-6361:20031499)
- Plume, R., Bensch, F., Howe, J. E., et al. 2000, *ApJL*, 539, L133, doi: [10.1086/312847](https://doi.org/10.1086/312847)

- Popping, G., Decarli, R., Man, A. W. S., et al. 2017, *A&A*, 602, A11, doi: [10.1051/0004-6361/201730391](https://doi.org/10.1051/0004-6361/201730391)
- Privon, G. C., Ricci, C., Aalto, S., et al. 2020, *ApJ*, 893, 149, doi: [10.3847/1538-4357/ab8015](https://doi.org/10.3847/1538-4357/ab8015)
- Sakamoto, K., Aalto, S., Costagliola, F., et al. 2013, *ApJ*, 764, 42, doi: [10.1088/0004-637X/764/1/42](https://doi.org/10.1088/0004-637X/764/1/42)
- Salak, D., Nakai, N., Seta, M., & Miyamoto, Y. 2019, *ApJ*, 887, 143, doi: [10.3847/1538-4357/ab55dc](https://doi.org/10.3847/1538-4357/ab55dc)
- Sanders, D. B., Mazzarella, J. M., Kim, D. C., Surace, J. A., & Soifer, B. T. 2003, *AJ*, 126, 1607, doi: [10.1086/376841](https://doi.org/10.1086/376841)
- Sandstrom, K. M., Leroy, A. K., Walter, F., et al. 2013, *ApJ*, 777, 5, doi: [10.1088/0004-637X/777/1/5](https://doi.org/10.1088/0004-637X/777/1/5)
- Sault, R. J., Teuben, P. J., & Wright, M. C. H. 1995, *Astronomical Society of the Pacific Conference Series*, Vol. 77, *A Retrospective View of MIRIAD*, ed. R. A. Shaw, H. E. Payne, & J. J. E. Hayes (San Francisco, CA: ASP), 433
- Schinnerer, E., Eckart, A., Tacconi, L. J., Genzel, R., & Downes, D. 2000, *ApJ*, 533, 850, doi: [10.1086/308702](https://doi.org/10.1086/308702)
- Schleicher, D. R. G., Spaans, M., & Klessen, R. S. 2010, *A&A*, 513, A7, doi: [10.1051/0004-6361/200913467](https://doi.org/10.1051/0004-6361/200913467)
- Schöier, F. L., van der Tak, F. F. S., van Dishoeck, E. F., & Black, J. H. 2005, *A&A*, 432, 369, doi: [10.1051/0004-6361:20041729](https://doi.org/10.1051/0004-6361:20041729)
- Scoville, N. Z., Evans, A. S., Thompson, R., et al. 2000, *AJ*, 119, 991, doi: [10.1086/301248](https://doi.org/10.1086/301248)
- Shimajiri, Y., Sakai, T., Tsukagoshi, T., et al. 2013, *ApJL*, 774, L20, doi: [10.1088/2041-8205/774/2/L20](https://doi.org/10.1088/2041-8205/774/2/L20)
- Soifer, B. T., Bock, J. J., Marsh, K., et al. 2003, *AJ*, 126, 143, doi: [10.1086/375647](https://doi.org/10.1086/375647)
- Solomon, P. M., & Vanden Bout, P. A. 2005, *ARA&A*, 43, 677, doi: [10.1146/annurev.astro.43.051804.102221](https://doi.org/10.1146/annurev.astro.43.051804.102221)
- Stoerzer, H., Stutzki, J., & Sternberg, A. 1997, *A&A*, 323, L13
- Supanitsky, A. D., & de Souza, V. 2013, *JCAP*, 2013, 023, doi: [10.1088/1475-7516/2013/12/023](https://doi.org/10.1088/1475-7516/2013/12/023)
- Tacconi, L. J., Genzel, R., Blietz, M., et al. 1994, *ApJL*, 426, L77, doi: [10.1086/187344](https://doi.org/10.1086/187344)
- Tang, X. D., Henkel, C., Menten, K. M., et al. 2019, *A&A*, 629, A6, doi: [10.1051/0004-6361/201935603](https://doi.org/10.1051/0004-6361/201935603)
- Tauber, J. A., Lis, D. C., Keene, J., Schilke, P., & Buettgenbach, T. H. 1995, *A&A*, 297, 567
- Valentino, F., Magdis, G. E., Daddi, E., et al. 2018, *ApJ*, 869, 27, doi: [10.3847/1538-4357/aaeb88](https://doi.org/10.3847/1538-4357/aaeb88)
- . 2020, *ApJ*, 890, 24, doi: [10.3847/1538-4357/ab6603](https://doi.org/10.3847/1538-4357/ab6603)
- van der Tak, F. F. S., Black, J. H., Schöier, F. L., Jansen, D. J., & van Dishoeck, E. F. 2007, *A&A*, 468, 627, doi: [10.1051/0004-6361:20066820](https://doi.org/10.1051/0004-6361:20066820)
- van Dishoeck, E. F., & Black, J. H. 1988, *ApJ*, 334, 771, doi: [10.1086/166877](https://doi.org/10.1086/166877)
- Viti, S., García-Burillo, S., Fuente, A., et al. 2014, *A&A*, 570, A28, doi: [10.1051/0004-6361/201424116](https://doi.org/10.1051/0004-6361/201424116)
- Wada, K., Fukushige, R., Izumi, T., & Tomisaka, K. 2018, *ApJ*, 852, 88, doi: [10.3847/1538-4357/aa9e53](https://doi.org/10.3847/1538-4357/aa9e53)
- Walter, F., Weiß, A., Downes, D., Decarli, R., & Henkel, C. 2011, *ApJ*, 730, 18, doi: [10.1088/0004-637X/730/1/18](https://doi.org/10.1088/0004-637X/730/1/18)
- Weiß, A., Henkel, C., Downes, D., & Walter, F. 2003, *A&A*, 409, L41, doi: [10.1051/0004-6361:20031337](https://doi.org/10.1051/0004-6361:20031337)
- Wilson, A. S., Helfer, T. T., Haniff, C. A., & Ward, M. J. 1991, *ApJ*, 381, 79, doi: [10.1086/170630](https://doi.org/10.1086/170630)
- Wright, E. L., Mather, J. C., Bennett, C. L., et al. 1991, *ApJ*, 381, 200, doi: [10.1086/170641](https://doi.org/10.1086/170641)